**Alma Mater Studiorum - Università di Bologna**

School of Science
Department of Physics and Astronomy
Master Degree Programme in Astrophysics and Cosmology

# Efficiency of the rapid neutron-capture process in the Large Magellanic Cloud

Graduation Thesis

Presented by:
**Elena Bernabini**

Supervisor:
**Prof.
Alessio Mucciarelli**

Academic Year 2025-2026
Graduation date I

# Abstract

Most of the elements heavier than Fe are produced by neutron-capture processes, which can be slow or rapid (s- and r-processes).
Currently, r-process nucleosynthesis sites are thought to be rare and stochastic, and mainly associated with neutron star mergers or rare core-collapse supernovae. However, understanding the precise sites of production of the r-process is still one of the major challenges in modern stellar astrophysics, as the details of this mechanism are not fully known yet.
Among r-process elements, Europium is almost completely produced by this mechanism. For this reason, the measurement of Eu abundance in stars is commonly used as a tracer of the rapid neutron-capture nucleosynthesis in different environments, both in the Milky Way and in other galaxies of the Local Group.
Recent studies have suggested that accreted stars in the Milky Way have higher [Eu/Fe] and [Eu/$\alpha$] abundance ratios with respect to stars formed in situ. This finding indicates a stronger efficiency of the r-process in the parent galaxies where these stars originally formed (likely dissolved systems, such as dwarf spheroidal or ultra-faint dwarf galaxies).
For this reason, in the context of Galactic Archaeology, the measure of Eu abundances in different Local Group galaxies such as the Magellanic Clouds is crucial to understand the assembly history of the Milky Way. Despite their proximity, the Magellanic Clouds have been poorly studied concerning these abundances. Only recently, Eu abundances of the Small Magellanic Cloud have been measured, demonstrating that this galaxy produced r-process elements more efficiently than $\alpha-$capture elements.
The aim of this work is to compare the efficiency of production of $\alpha-$elements, rapid, and slow neutron-capture elements in the Large Magellanic Cloud and Small Magellanic Cloud, in order to understand if the two galaxies exhibit a similar behaviour or possible differences due to their different chemical enrichment histories.
With the goal of removing any systematics that can affect different chemical analyses, and to ensure a consistent comparison, we re-analysed a sample of 113 red giant branch stars in the Large Magellanic Cloud (Van der Swaelmen et al., 2013) but adopting the same procedures and assumptions that were used for the Small Magellanic Cloud (Anoardo et al., 2026). Using the photometric data from the Gaia Data Release 3 and high-resolution spectra acquired with the multi-object spectrograph FLAMES at the VLT, we derived the abundance ratios for Fe, Eu, Mg and Ba.
In both Magellanic Clouds, [Mg/Fe] abundances reflect the slower star formation of the relative galaxy with respect to the Milky Way. On the other hand, stars from the Large Magellanic Cloud exhibit enhanced [Eu/Fe] values, similarly to stars from

the Small Magellanic Cloud at the same metallicities, indicating that the r-process is slightly enhanced with respect to the Milky Way.
Moreover, [Eu/Mg] is found to be systematically higher than in Milky Way stars and appears to be compatible with the Small Magellanic Cloud, proving a stronger efficiency of the r-process with respect to the $\alpha-$capture process.
Lastly, [Ba/Fe] and [Ba/Eu] abundances demonstrate that the s-process is dominant with respect to the r-process in the Magellanic Clouds.
This homogeneous comparison between the Large Magellanic Cloud and the Small Magellanic Cloud allows to better understand the r-process enrichment in these two galaxies, indicating that in environments with a lower star formation efficiency than the Milky Way, the r-process is extremely efficient and stronger than the $\alpha-$capture process.
Finally, this work confirms that [Eu/Mg] can be a powerful tool for chemical tagging in the Milky Way, to distinguish between stars that formed in situ and stars that were accreted from nearby systems.

# Contents

# Chapter 1

# Introduction

## 1.1 Europium and the rapid neutron-capture process

The Big Bang nucleosynthesis produced H, He, and small amounts of Li. All the other metals are produced mainly in stars, through thermonuclear burning or neutron-capture processes. Specifically, the latter are responsible for the production of most of the elements heavier than Fe in the Universe, as shown in Fig. 1.1 (Cowan et al., 2021).
These processes occur when atomic nuclei capture free neutrons and subsequently undergo $\beta-$decay to reach a stable configuration, producing ultimately a heavier element (Gallino et al., 1998; Busso et al., 1999).
The sequence of neutron capture for a nucleus $Z^A$ and the following $\beta-$decay can be summarized as follows:

$$Z^A + n \rightarrow Z^{A+1}$$

$$n \rightarrow p^+ + e^- + \bar{\nu}_e$$

$$Z^{A+1} \rightarrow Z + 1^{A+1}$$

Depending on the relative timescales between the neutron capture and the $\beta-$decay, as well as the availability of free neutrons, these processes can be divided into:

1. The slow neutron-capture process (hereafter referred to as s-process) which occurs at intermediate or moderate neutron densities ($\sim 10^{7-12}$ $neutrons/cm^3$), when each neutron capture is followed by a $\beta-$decay (Busso et al., 1999; Gallino et al., 1998). This process produces most of the total amount of elements like Barium and Lanthanum and is generally associated with intermediate-mass ($\sim 2-4\ M_\odot$) asymptotic giant branch stars (Busso et al., 1999; Cristallo et al., 2015). Timescales can range from $10^2$ to $10^5$ $yrs$ (Burbidge et al., 1957).

2. The rapid neutron-capture process (hereafter referred to as r-process) which is associated with extreme neutron fluxes, with densities of $\sim 10^{20}$ $neutrons/cm^3$, where multiple neutrons are captured on timescales significantly shorter than those of the $\beta-$decay (Cowan et al., 2021; Arcones & Thielemann, 2023; Thielemann & Cowan, 2026). In this case, the $\beta-$decay only occurs afterwards,

bringing the nuclei back to the valley of stability. Observations also suggest a distinction between weak and strong r-process, respectively producing lighter or heavier r-elements.

Among rapid neutron-capture elements, Europium is widely used as a tracer of the r-process because it is produced almost entirely through this mechanism. As a matter of fact, Arlandini et al. (1999) estimated that for the Sun $\sim 94\%$ of the Eu is produced by the r-process.
For this reason, most of the information that we have about the efficiency of the r-process comes from the measurements of Eu abundances in stellar atmospheres.

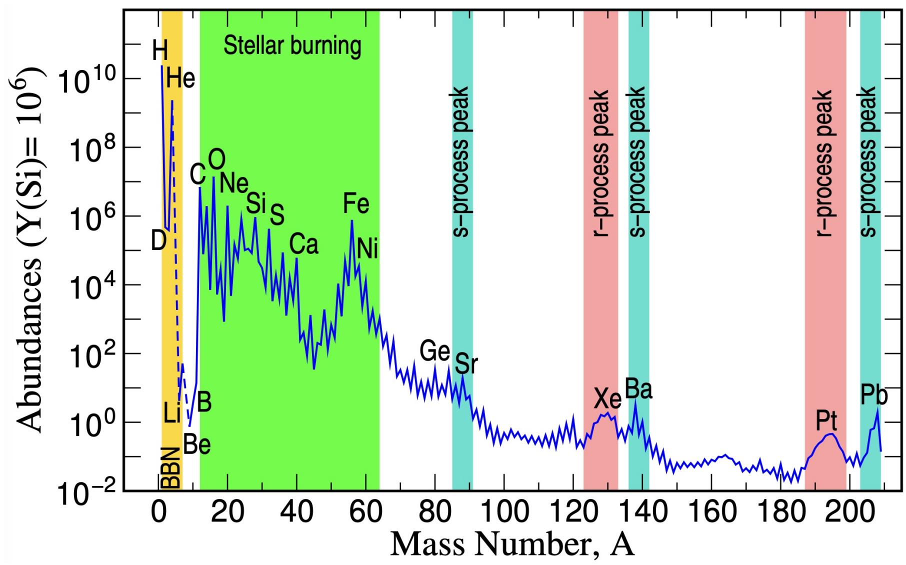


**Figure 1.1:** Contributions to the abundances of different elements and their isotopes in the solar system, highlighting the main nucleosynthesis mechanisms. The Big Bang nucleosynthesis is responsible for the lightest elements, H, He, Li, then stellar burning produces elements up to the Fe peak, and finally neutron-capture processes produce the heavier elements. Some small contributions to the heavier elements also come from p, $\nu$ and $\nu$-p processes. From Cowan et al. (2021).

## 1.2 Astrophysical sites of r-process

Several studies (Cowan et al., 2021; Arcones & Thielemann, 2023; Thielemann & Cowan, 2026) have discussed the possible astrophysical sites for the production of r-elements.
Potential scenarios, which generally involve the creation of a neutron star (NS) after a core-collapse supernova (CC-SNe) explosion, for stars between $\sim 8$ and $\sim 25\ M_{\odot}$, or NS mergers, involve very dense and hot matter, cooling through neutrino emission. Specifically, electron anti-neutrinos can interact with matter and convert it into neutron-rich.

$$\bar{\nu}_e + p \rightleftharpoons n + e^+$$

Models explaining possible sites of r-process are still being developed, as simulations are complex, involving relativistic, magneto-hydrodynamic, and nuclear physics subjects. Potential scenarios are discussed in the following sections.

### 1.2.1 Compact binary sources

In the context of r-process nucleosynthesis, the term compact binary merger refers to the outcome of the evolution of a binary system made of two compact objects, where at least one is a neutron star (either two NSs, or a NS and a black hole). This class of events was proposed as an efficient production site of r-process in the 1970s (Lattimer & Schramm, 1974).
A compact binary merger can be associated with the detection of a gravitational wave, since during the inspiral phase the two bodies grow closer and lose gravitational orbital energy, thus emitting gravitational waves.
In particular, since a NS is involved in the merger, the observation of an electromagnetic counterpart is expected following the gravitational wave detection. The extremely energetic electromagnetic emission that is observed is called kilonova and it can be accompanied by short-duration gamma-ray bursts, transient emissions characterized by a rapid flash of gamma rays.
Kilonovas emit across the whole electromagnetic spectrum and observations of radioactive decays indicate the presence of heavy r-process nuclei from the mass accretion on the NS or black hole.
The observation of the gravitational wave event GW170817 (Abbott et al., 2017) and the subsequent kilonova, has demonstrated for the first time that this kind of events produce a significant amount of r-process elements (Pian et al., 2017; Watson et al., 2019).
An estimate of the r-process mass produced in compact binary mergers is of the order of 0.01 $M_{\odot}$ per event (Cowan et al., 2021). However, this contribution is quite delayed with respect to the first CC-SNe, due to the timescale of the process that can take as long as $10^8 - 10^9$ $yrs$. Consequently, this scenario may not have been a primary contributor to the r-process in the early stages, requiring additional sources at metallicities [Fe/H]$< -2$ dex.
Nevertheless, NS mergers are definitely responsible for the r-process at later times, contributing to the explanation of the pattern of [Eu/Fe] at metallicities [Fe/H]$> -2$ dex, as well as the decline of [Eu/Fe].
Matteucci et al. (2014) calculated chemical evolution models for [Eu/Fe] in the Milky Way, evaluating the different sources of r-process. They demonstrated that NS mergers can reproduce the observed abundances in the Milky Way, but only assuming a short and constant delay time for the merging. Otherwise, with a different delay time distribution between star formation and merger, the observed chemical patterns could be reproduced only if other sources of r-process were included (Molero et al., 2023).

### 1.2.2 Magneto-rotational core-collapse SNe

For extremely metal-poor stars, a more likely contributor to the r-process is represented by magneto-rotational CC-SNe (MHD-SNe) (Reichert et al., 2021; Mösta et al., 2018). In this scenario, the SN explosion is triggered by strong magnetic fields and fast rotation of the stellar core, and results in a NS remnant with an intense magnetic field ($\sim 10^{12} - 10^{13}\ G$).
The process is able to produce a wide range of r-elements, from weak to strong, depending on the initial conditions. For small magnetic fields, weak r-elements or no r-elements at all can be produced.
According to Cowan et al. (2021), this scenario could be in act early enough to explain the scatter of r-elements in low metallicity stars. However, this rare CC-SNe should account for $\sim 1\%$ of all the stars exploding as standard CC-SNe (Woosley & Heger, 2006) and they should not be able to reproduce the total amount of observed r-process elements.

### 1.2.3 Collapsars

Collapsars are the result of the final collapse of massive stars that ends in a black hole accreting matter, a specific kind of SNe characterised by high kinetic energies, and that can also be associated with long-duration gamma ray bursts.
Under specific requirements, collapsars can create a neutron rich environment and co-produce Fe and large amounts of r-process nuclei, for a mass greater than 0.1 $M_\odot$ (Cowan et al., 2021). However, this co-production of Fe and r-process elements alone would not be sufficient to explain the decreasing trend observed in the behaviour of [Eu/Fe] as a function of [Fe/H].
Given such high mass yields, a frequency of one collapsar per $10^3 - 10^4$ regular CC-SNe could explain the solar r-process abundances. Similarly to MHD-SNe, collapsars can also be responsible for the production of r-process at early times, however, they seem less likely due to the stringent requirements (Soker, 2026).

### 1.2.4 Common envelope jets SNe

A common envelope jets supernova (CEJSN) is a process in which a NS enters the core of a massive star and accretes mass rapidly, creating a neutron rich accretion disc that is driving the r-process. In this scenario jets are also launched, possibly carrying away the r-elements.
If the NS collapses, mass accretion can continue on the newly formed black hole, so that the r-process production can keep going. The estimated r-process mass yield of the continued accretion on the black hole is very large, of the order of 0.1 $M_\odot$ (Soker, 2026).
The timescale of this process is somewhat close to that of regular CC-SNe, with only a small delay, thus representing a significant contribution to the r-process at early times. Soker (2026) speculates that CEJSNe may be responsible not only for the production of the heavier r-elements at early times, but also for the synthesis of lighter r-process nuclei.

As a result, the most likely scenario is one in which different sources act on different timescales (Anoardo et al., 2026). The primary contribution to the r-process at early times is possibly a combination of CEJSNe for heavier nuclei and MHD-SNe. Alongside, there are the less likely contributions from collapsars, for lighter nuclei, and the small contribution from compact binary mergers for heavier nuclei. Compact binary mergers, however, definitely contribute at later times.

## 1.3 [Eu/Fe] in the Milky Way

As discussed above, Europium is one of the purest r-process elements that we can measure in stellar spectra. Most of the information about r-process efficiency in the Milky Way and in other resolved stellar systems comes from the [Eu/Fe] abundance ratios.
Figure 1.2 shows the behaviour of [Eu/Fe] as a function of [Fe/H] for Milky Way stars over a large range of metallicities (Cowan et al., 2021).

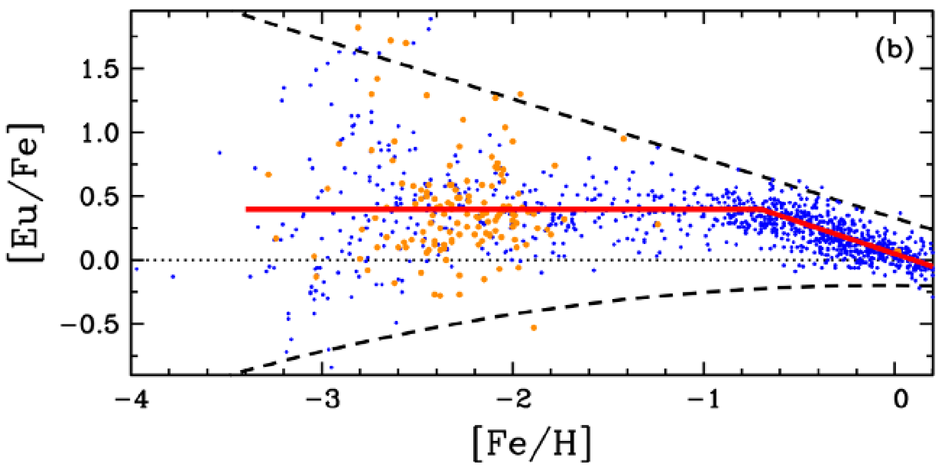


**Figure 1.2:** [Eu/Fe] abundances as a function of [Fe/H] for Milky Way stars, highlighting the large scatter and the following decreasing behaviour. The red solid lines represent the overall trend of the stars, the black dashed lines highlight the typical star-to-star scatter at any metallicity. From Cowan et al. (2021).

The first noticeable feature is the existence of a large scatter at very low metallicities, [Fe/H]$\lesssim -2$ dex, with stars reaching extreme values, as low as [Eu/Fe]$\sim -0.8$ dex and as high as $\sim +2$ dex. This spread, which is much larger than the uncertainties associated to the measured abundances, reflects the stochastic nature of the astrophysical sites of the early r-process, suggesting that the latter may have happened in a gas that was not mixed homogeneously. The presence of some Fe in the stars also indicates a short delay with respect to the first CC-SNe, injecting small amounts of Fe in the interstellar medium (ISM).
As well as a low frequency of the events generating the r-process, also a large r-element production per individual event, $> 0.1\ M_\odot$, is required to reproduce this scatter (Soker, 2026).
The scatter begins to decrease only as metallicity increases, around [Fe/H]$\gtrsim -1.5$

dex, where [Eu/Fe] reaches a super-solar average value, indicating that the enrichment is efficient.
Finally, a clear decreasing trend for [Eu/Fe] is seen starting from [Fe/H]$\geq -1$ dex, indicating the onset of SNe Ia injecting Fe in the ISM and not producing any r-elements.

## 1.4 [Eu/Fe] in dwarf-spheroidal and ultra-faint galaxies

Different studies have been conducted to understand neutron-capture processes in dwarf spheroidal (dSph) galaxies.
Reichert et al. (2020) present a study of 13 dwarf spheroidal and ultra faint galaxies, involving 380 stars from Fornax, Sagittarius, Sculptor, Sextans, Carina, Ursa Minor, Draco, Reticulum II, Bootes I, Ursa Major II, Lei I, Segue I and Triangulum II. The goal is to compare the different relative abundances of s- and r-process elements.
For example, the behaviour of [Eu/Ba] against [Ba/H] shows at first a slope of $\sim 1$, indicating that Ba is initially produced with Eu through the r-process. The following decrease indicates the onset of Ba production from the s-process in asymptotic giant branch (AGB) stars, which is expected to have a time delay similar to that of SNe Ia. Evidence of r-process elements before the first SNe Ia points to the need for an additional early r-process site, other than the compact binary mergers.
Focusing on the trend of r-process elements versus $\alpha-$elements, models that implement the r-process only through NS mergers are expected to have a positive slope, due to the long time delay with respect to CC-SNe. A flatter behaviour is expected if r-process production sites also involve sources with time delay similar to CC-SNe. Observations for Sagittarius support the contribution of rare CC-SNe like sources to the r-process.
Finally, the behaviour of [Eu/Fe] in the Milky Way seen in Fig. 1.2, showing a plateau followed by a decreasing trend, is also seen in dSphs like Sagittarius, Fornax, Sculptor, Sextans. It is explained as the result of an additional source of r-process in the early universe creating the plateau, and the contribution of NS mergers at a delayed time generating the decrease.

Regarding the Local Group, works on dwarf spheroidal galaxies to model the Eu enrichment have been proposed. These galaxies are characterized by metallicities of the order of [Fe/H]$\lesssim -2, -3$ dex, and thanks to their closeness to the Milky Way, they serve as perfect grounds to study the chemical evolution of the r-process at low metallicities.
Palla et al. (2025) aim at comparing model predictions for three of the most massive dSphs in the Local Group, Sagittarius (Sgr), Fornax (For) and Sculptor (Scl), with the Milky Way. Before building the chemical evolution models, data about the abundances are collected and examined, focusing on the patterns of [Eu/Fe] and [Eu/Mg] in the various galaxies, representing the relative Eu abundance with respect to Fe and $\alpha$-elements. Two main differences are observed:

1. The pattern of [Eu/Fe] vs [Fe/H] is similar among the Milky Way, For and Sgr (as shown for the latter in the bottom panel in Fig. 1.3). Scl has an overall

lowered abundance of [Eu/Fe];

2. The pattern of [Eu/Mg] vs [Fe/H] is similar between Scl and the Milky Way, while it is enhanced for Sgr and For.

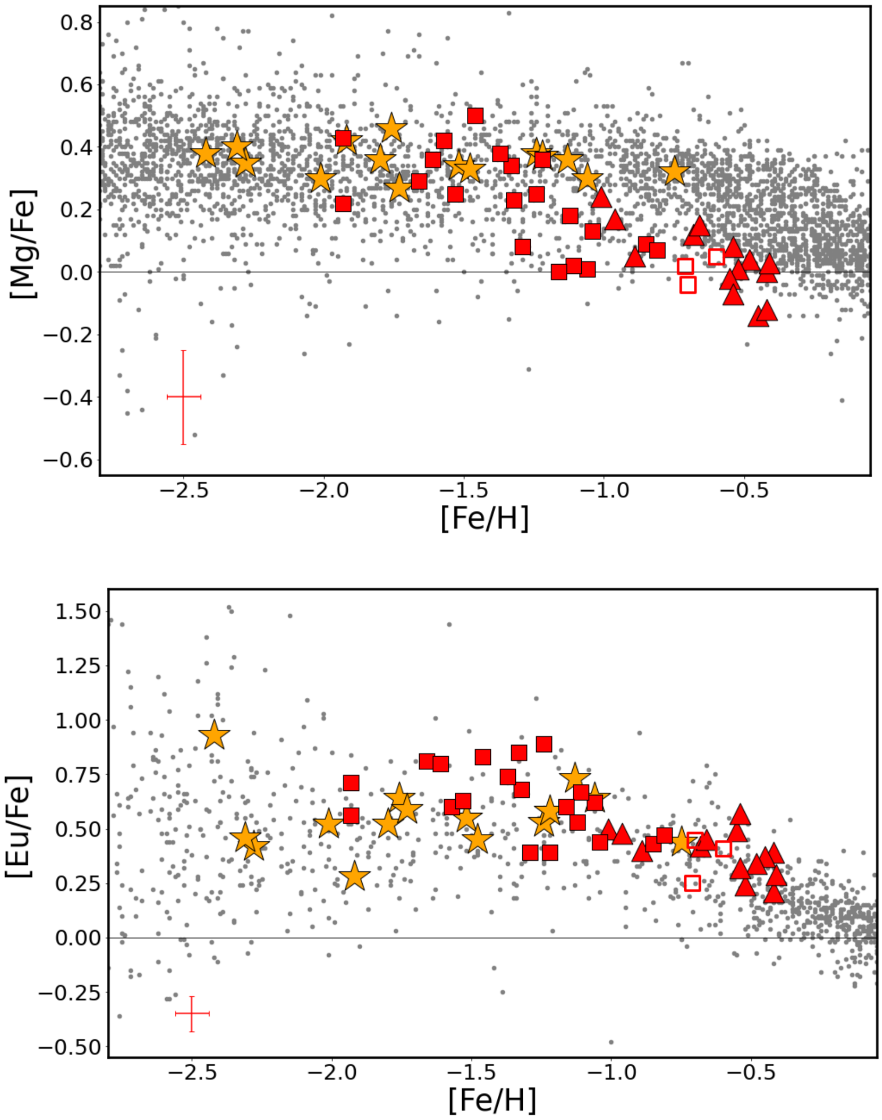


**Figure 1.3:** [Mg/Fe] and [Eu/Fe] abundances in the stars of the Sagittarius dwarf spheroidal galaxy: the top panel shows the behaviour of [Mg/Fe] as a function of [Fe/H], while the bottom panel shows [Eu/Fe] as a function of [Fe/H]. Gray circles represent Milky Way field stars from the SAGA database (Suda et al., 2008), orange stars are Milky Way globular cluster analysed by Mucciarelli et al. (2023) and red squares and triangles represent stars from the Sagittarius dwarf spheroidal galaxy. From Liberatori et al. (2025)

Chemical evolution models are then built with the goal of explaining these differences, starting from the individual star formation histories of the galaxies.
Then, r-process nucleosynthesis is implemented through two channels, a prompt one, the magneto-rotational CC-SNe, and a delayed one, the compact binary mergers,

with mass yields consistent with Eu abundances in the Milky Way.
Model results are found be representative of the Milky Way data over a wide range of metallicities, proving the necessity of two sources of r-process nucleosynthesis: the prompt one, being the dominant channel, and the delayed, contributing to a negligible amount.
On the other hand, results are lacking in Eu abundance for the three dSphs by almost 0.5 dex. The models can be reconciled with the data, only by increasing by a factor 4 the Eu production rate. The missing Eu could be delivered from either of the two production channels. The hypothesis of increasing the Eu production at low metallicities from delayed sources is proposed as the more reasonable option.
The fact that significantly different Eu production procedures need to be applied, proves that the same r-process enrichment scenario cannot work simultaneously for the Milky Way and the dwarf galaxies.

Among dSphs in the Local Group, the Magellanic Clouds are a system of two closely interacting galaxies, the Small Magellanic Cloud (SMC), and the Large Magellanic Cloud (LMC). Their gravitational and hydrodynamical interaction can be seen through the Magellanic Stream, wrapping the two galaxies, and the Magellanic Bridge, connecting them and allowing mass exchange.
The SMC and LMC are the two most massive satellites of the Milky Way in the Local Group, with the LMC having a mass between 1 and $3 \cdot 10^{11}\ M_{\odot}$ and a stellar mass of $\sim 10^9\ M_{\odot}$ (van der Marel & Kallivayalil, 2014; Erkal et al., 2019), and the SMC having a total mass of $\sim 3 \cdot 10^9\ M_{\odot}$ and a stellar mass of $\sim 5 \cdot 10^8\ M_{\odot}$ (Rubele et al., 2018; Stanimirović et al., 2004).
Furthermore, their close proximity to the Galaxy, at a distance of $\sim 50\ kpc$ and $\sim 60\ kpc$ for the LMC and SMC respectively, offers the chance to study resolved stars from systems that are currently interacting with the Milky Way.

Although several studies based on high-resolution spectroscopy have investigated the chemical composition of the Magellanic Clouds (Pompéia et al., 2008; Van der Swaelmen et al., 2013; Nidever et al., 2020; Hasselquist et al., 2021; Mucciarelli et al., 2023), the measurement of the Eu abundance in these galaxies has received limited attention. In the case of the SMC, only recently, the first Eu abundances have been derived (Anoardo et al., 2026).
Regarding the LMC, the inner disc chemical abundances were studied by Pompéia et al. (2008), to investigate the star formation and evolution of the galaxy.
Among the main results, it is proved that the overall abundance patterns of different elements in dSphs seem to differ from those of the Milky Way halo. In general, elemental abundances seem to be lower than in the Milky Way, indicating a slower stellar evolution in the LMC.
Given that [$\alpha$/Fe] abundance ratios appear decreased in the LMC, a possible explanation is a slower development of the star formation with respect to the Milky Way, with a higher frequency of SNe Ia with respect to SNe II, and possibly a steeper initial mass function.
S-elements were also studied, finding the lighter elements underabundant and the heavier elements slightly enhanced. This result is possibly explained considering s-element production from AGB stars being metallicity dependent.

Finally, in Van der Swaelmen et al. (2013), LMC bar stars were analysed to derive radial velocities and metallicities.
Again, $\alpha-$elements abundances are found to be lower than in the Milky Way due to a higher enrichment of the ISM from SNe Ia. Elements like Si, Ca, Ti are produced more or less efficiently depending on the mass of the SNe II progenitor, while O and Mg are mainly produced by massive SNe II and only in little amounts by SNe Ia. The fact that Si, Ca and Ti overlap the Milky Way patterns, while O and Mg are decreased with respect to the Milky Way values (see Fig. 1.4) proves that the LMC formed high mass stars less efficiently than the Milky Way.

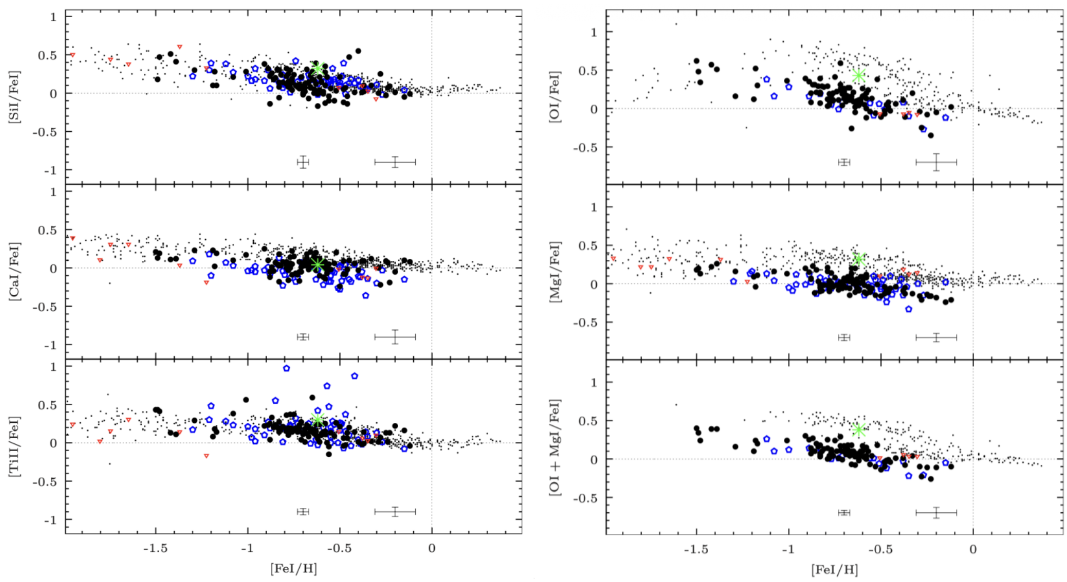


**Figure 1.4:** In the left panel: first row shows [Si I/Fe I] vs. [Fe/H], second row shows [Ca I/Fe I] vs. [Fe/H], third row shows [Ti II/Fe I] vs. [Fe/H]. In the right panel: first row shows [O I/Fe I] vs. [Fe/H], second row shows [Mg I/Fe I] vs. [Fe/H], third row shows [O I+Mg I/Fe I] vs. [Fe/H]. The black filled circles and blue open pentagons represent respectively LMC bar and disc stars from Van der Swaelmen et al. (2013); green asterisks represent Arcturus stars; red downward triangles are for LMC globular clusters (Johnson et al. 2006; Mucciarelli et al. 2008, 2010); black tiny dots represent Milky Way thin and thick disc (Bensby et al. 2005; Reddy et al. 2003, 2006), halo (Fulbright 2000; Stephens & Boesgaard 2002; Reddy et al. 2006), and additional Milky Way data for O from Carretta et al. (2000). Typical random (left) and systematic (right) error bars on both coordinates are provided for the LMC samples. From Van der Swaelmen et al. (2013).

S-elements abundances are observed to increase with metallicity and to be higher than in the Milky Way for [Fe/H]$> -1$ dex, indicating a more efficient production of s-elements in AGB stars.
The Eu abundance is found to be higher than in the Milky Way at [Fe/H]$> -1$ dex. In this article, the enhancement in Eu abundances is thought to be produced either by a third source of r-processes, other than NS and SNe II, or some kind of s-process in carbon enhanced metal poor stars which exhibit both r- and s-process elements.

Regarding the SMC, the overall chemistry of the galaxy seems to be distinct from

that of the Milky Way (Mucciarelli et al., 2023) showing higher [r/Fe] abundance ratios and lower [$\alpha$/Fe] abundance ratios at the same metallicity.
New chemical evolution models for the galaxy have also been developed, with detailed implementation of many nucleosynthesis mechanisms, focusing on the elements produced by neutron-capture processes. Model predictions have been compared with observations and seem to severely underestimate the patterns of both neutron capture processes. It seems that models require a boost by a factor 4 on the production of r-elements at low metallicities from NS mergers, as suggested in Palla et al. (2025), and possibly the adoption of a top lighter initial mass function to help reconcile the trends (Palla et al., 2026).
According to Anoardo et al. (2026), the enhancement of the r-process (see Fig. 1.5) could support the idea to use [Eu/$\alpha$] for chemical tagging on intermediate and high metallicity stars in the Milky Way halo.

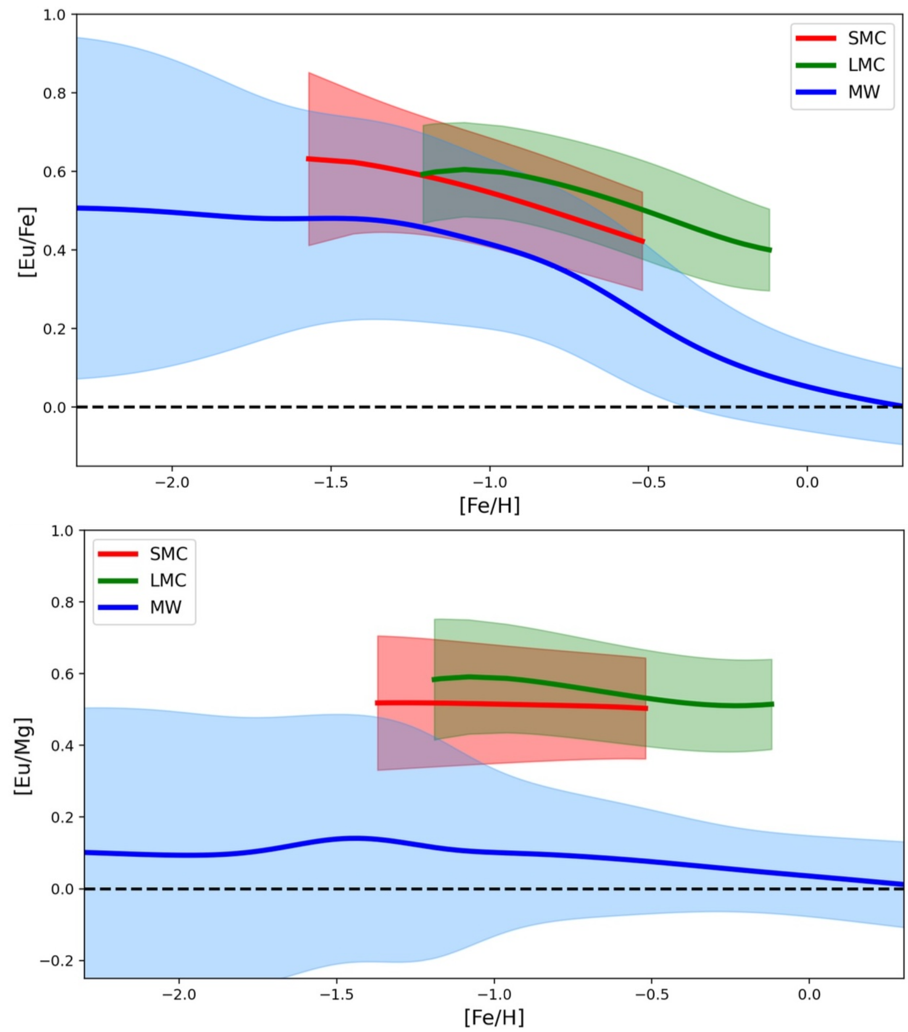


**Figure 1.5:** In the top and bottom panels the trends for [Eu/Fe] and [Eu/Mg] as a function of [Fe/H] are shown. The red line represents results for the SMC from Anoardo et al. (2026), the blue line represents data from the Milky Way (collected from the SAGA database, Suda et al., 2008), and the green line represents the abundances for LMC stars (from Van der Swaelmen et al., 2013).

Several works performed so far on Local group galaxies smaller than the Milky Way (therefore with a lower star formation efficiency) indicate that these systems can have, at the highest metallicties, [Eu/$\alpha$] abundance ratios significantly higher than those measured for Milky Way stars of similar [Fe/H]. Consequently, different authors (Monty et al., 2024; Ceccarelli et al., 2024; Anoardo et al., 2026) have proposed the use of this kind of abundance ratio to discriminate between accreted and in situ stars in the Milky Way. In fact, stars dynamically associated to accretion events in the Galaxy exhibit systematically higher [Eu/Si] abundance ratios (as shown in Fig. 1.6 and 1.7).
Finally, the SMC matches this behaviour, showing [Eu/Fe] values measured by Anoardo et al. (2026) compatible with the Milky Way stars, while the two galaxies differ for [Mg/Fe]. Therefore, the SMC stars result to have higher [Eu/Mg] with respect to the Milky Way.

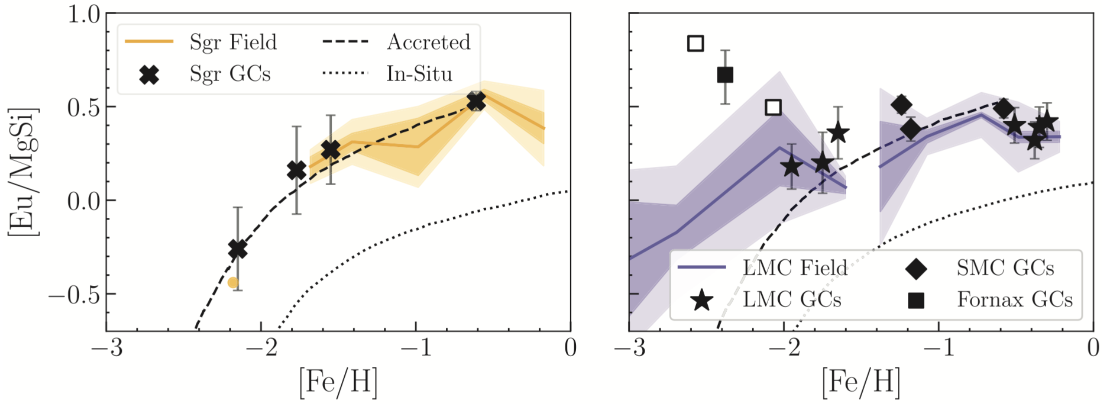


**Figure 1.6:** In the left panel the binned mean abundance values of [Eu/Mg] versus [Fe/H] for Sgr field stars from Reichert et al. (2020) in are shown in yellow. The dark and light shaded regions represent respectively the median absolute deviation weighted by square root the number of stars per bin and 1$\sigma$ times the median absolute deviation. In the right panel the binned mean abundance and dispersion for LMC field stars from the studies of Oh et al. (2024), Reggiani et al. (2021), Van der Swaelmen et al. (2013) and Pompéia et al. (2008) are shown in purple. LMC globular clusters from the studies of Mucciarelli et al. (2008) and Mucciarelli, Origlia & Ferraro (2010) are overplotted as stars. The dashed and dotted black lines represent respectively chemical evolution models to reproduce the accreted and in situ stars. From Monty et al. (2024).

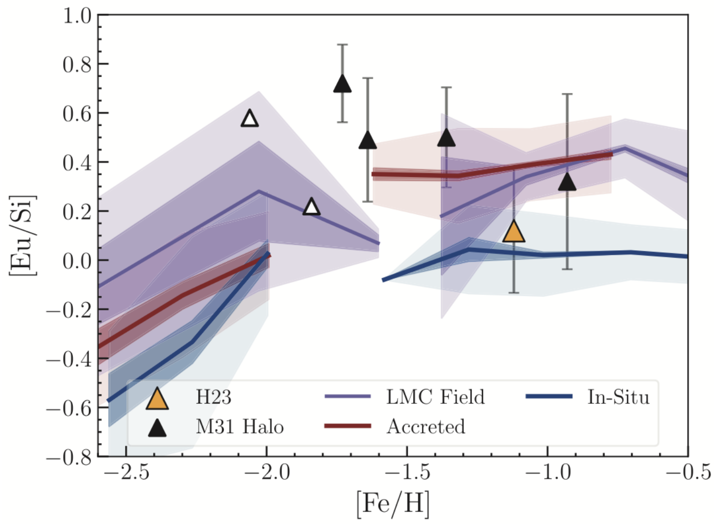


**Figure 1.7:** Distribution of [Eu/Si] as a function of metallicity for globular clusters in external galaxies. LMC, Milky Way (in situ), and Gaia-Sausage/Enceladus dwarf galaxy (accreted) field stars means are shown. The dark and light shaded regions represent respectively the median absolute deviation weighted by square root the number of stars per bin and $1\sigma$ times the median absolute deviation. From Monty et al. (2024).

## 1.5 The astrophysical problem: Eu abundance in the Magellanic Clouds

The goal of this thesis is to determine whether the LMC and SMC exhibit a similar behaviour in terms of Eu enrichment and r-elements production. In order to do this, one should compare results without possible systematic errors due to the different analysis methods.
Therefore, we will re-analyse the Eu abundance in the LMC stars studied in Van der Swaelmen et al. (2013), using methods that are consistent with those applied for the SMC in Anoardo et al. (2026). In particular, the LMC sample will be analysed with the same approach to derive the stellar parameters, the same model atmospheres, and the same line lists for the transitions of interest.
As a result, obtaining the chemical profile of LMC stars can provide insight into whether Eu can be used as a chemical tag to infer the possible accretion of LMC or LMC-like fragments in the Galaxy.
Ultimately, a comparison between the chemistry with other Local Group galaxies can improve the current knowledge on the evolution of the Milky Way, as the history of the Galaxy depends strongly on the interactions with the neighbouring systems (Pompéia et al., 2008).

In the following chapters, the analysis of Eu in the LMC stars will be described, starting from the photometric and spectroscopic data, the methods used to prepare the data, and then the chemical analysis itself.
Finally, results are interpreted and discussed, comparing with SMC and Milky Way abundances and drawing conclusions.

# Chapter 2

# The spectroscopic dataset

The targets of the analysis are 113 stars belonging to the inner bar of the LMC. The sampled stars belong to the bright region of the red giant branch (RGB).
The spectra were obtained with the multi-object spectrograph FLAMES at the Very Large Telescope of ESO. The LMC region that was observed was centered on the coordinates RA= 81.19321, DEC= −69.79278.
The photometric data were collected from the Gaia Data Release 3 from a region centered on the same coordinates.

## 2.1 The Gaia photometric data

Gaia is a space mission of the European Space Agency that has provided astrometric and photometric information for almost 2 billions of stars in the Milky Way and in the Local Group. In particular, for each star, Gaia provides three magnitudes, named G, BP and RP (transmission curves of the three filters are shown in Fig. 2.1).

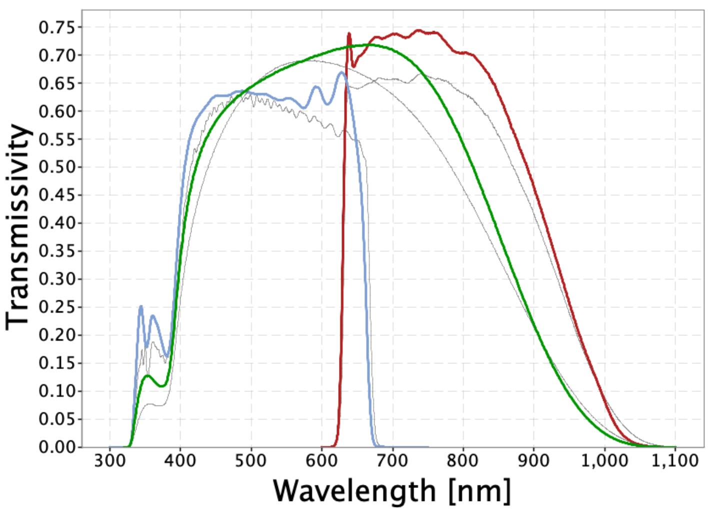


**Figure 2.1:** Gaia DR3 passbands. The coloured lines show the G, BP and RP passbands (green: G; blue: BP; red: RP), defining the Gaia photometric system. The thin, grey lines show the nominal, pre-launch passbands for Gaia DR1 (Jordi et al. 2010). Credits: ESA/Gaia/DPAC, P. Montegriffo, F. De Angeli, M. Bellazzini, E. Pancino, C. Cacciari, D. W. Evans, and CU5/PhotPipe team.

The photometric data for the targets were downloaded from the archive of the Gaia Data Release 3 (Gaia Collaboration et al., 2023), considering a spatial region of 17 arcmin of radius around the pointing centre of FLAMES.
In order to only keep the photometric data relative to the 113 spectroscopic targets, faint and main sequence stars were removed, restricting the original data to the brighter part of the RGB in the color magnitude diagram (CMD). This was performed considering stars for $15 < G < 17.5$ and $BP - RP > 0.7$.
At this point the match function in TOPCAT was used to only keep the Gaia data relative to the stars that need to be analysed, matching the sky coordinates with the data from Van der Swaelmen et al. (2013), as shown in the sky map in Fig. 2.2.
The final table with the photometric data downloaded from the Gaia archive contains the sky coordinates (RA, DEC), the parallax and proper motion, the three Gaia mean magnitudes in the G, BP and RP filters, with the respective errors on the fluxes, and the BP/RP excess factor for the 113 stars.
Figure 2.3 shows the CMD of the LMC bar stars, using the colour BP-RP on the x axis and the G magnitude on the y axis. The position of the spectroscopic targets of this analysis in the RGB is highlighted with respect to the field stars.

## 2.2 The 2MASS data

2MASS (Skrutskie et al., 2006) is an all-sky survey in the bands J, H, K, obtained from the virtual observatory option in TOPCAT. The data were downloaded from a circular region centered on the pointing centre of FLAMES with a radius of 16 arcmin. Again, using the stellar coordinates, only the data relative to the spectroscopic targets were kept.
As a result, the 2MASS table for the bar was obtained, containing the stellar ID, the sky coordinates, the J, K, H magnitudes with the relative error, and a flag describing the quality of the measured magnitudes.

## 2.3 The spectroscopic dataset

The spectra for the LMC bar stars were observed with FLAMES, a fiber-fed, multi-object echelle spectrograph on UT2 at VLT (Pasquini et al., 2000).
Using the GIRAFFE high resolution MEDUSA mode, three setups were considered for each star, HR11, HR13, HR14A. The latter setup, HR14A, is the one containing the Europium line at 6645 Å. The main characteristics of each setup, such as wavelength range, central wavelength and instrumental resolution are listed in table 2.1.
All the spectra were reduced using the dedicated ESO pipeline that performs bias-subtraction, flat-fielding, spectral extraction and wavelength calibration.
The spectra were also corrected for the contribution of the sky background using the median-average spectrum of some tens of GIRAFFE fibers dedicated to observe empty sky regions. Finally, the spectra were corrected for the heliocentric motion.
For all the target stars, the spectra for the three setups were available, except for two stars (named 05242198-6943579 and 05223082-6944147) for which HR11 and HR13 observations were not available respectively.

| | Wl start (Å) | Wl centre (Å) | Wl end (Å) | R (MEDUSA) |
|---|---|---|---|---|
| HR11 | 5597 | 5728 | 5840 | 29500 |
| HR13 | 6120 | 6273 | 6405 | 26400 |
| HR14A | 6308 | 6515 | 6701 | 18000 |

**Table 2.1:** Description of the setups used for the observation of the spectra, including wavelength range, central wavelength, and spectral resolution, obtained from the description of FLAMES in the ESO webpage.

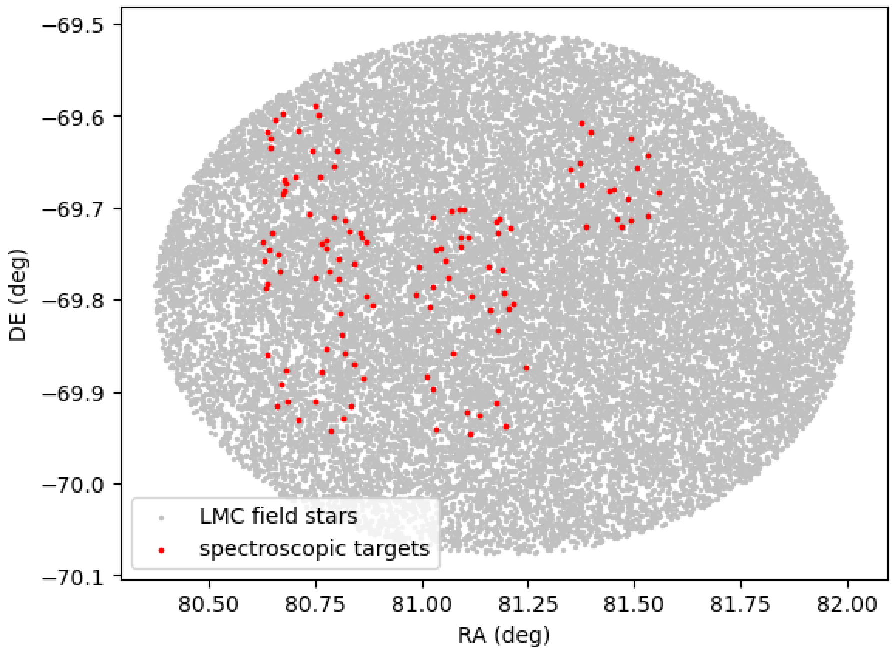


**Figure 2.2:** Sky map of the stellar sample from the LMC bar from the GAIA catalogue. The gray background represents the spatial distribution of the stars in a circular region of 17 arcmin centered on the pointing centre of FLAMES, while the red dots correspond to the stars selected for the analysis.

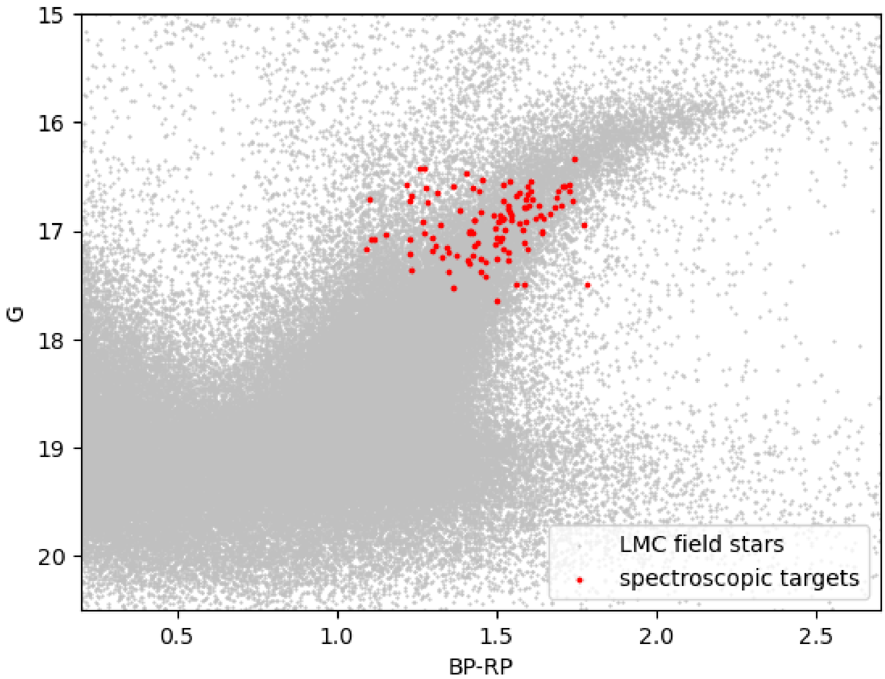


**Figure 2.3:** Colour-magnitude diagram of the stellar populations of the LMC bar. The data for the magnitudes were obtained from the GAIA Data Release 3, from the spatial region shown in the sky map in Fig. 2.2 (gray points). The red points are the FLAMES spectroscopic targets analysed in this study.

# Chapter 3

# Analysis methods

In this chapter, the methods used to prepare the data (such as normalization and radial velocity correction of the spectra), as well as the methods for the determination of the stellar parameters (effective temperature, surface gravity and microturbulent velocity) will be described.
Finally, the method to infer the chemical abundances of the stars of the FLAMES sample will be explained.

## 3.1 Determination of the colour excess

The first step to determine the stellar parameters is the estimate of the mean colour excess $E(B-V)$, in order to correct the photometric data for extinction.
The colour of a star is defined as the difference between the magnitude in two different photometric filters, and it is tightly linked with the stellar temperature. However, the observed colour is different from the intrinsic value, as it is affected by extinction, a strongly wavelength-dependent effect, caused by the presence of dust between the source and the observer.
The colour excess describes the effect of extinction on colours and is defined as the difference between the extinction in two bands, $E(B-V) = A_B - A_V$. Its value allows to determine the intrinsic colour of a star as $(B-V) = (B-V)_{obs} - E(B-V)$.
The mean colour excess in the direction of the FLAMES field analysed in this study has been obtained from the extinction maps for the Magellanic Clouds by Skorwon+21, that provide the color excess in terms of $E(V-I)$.
The derived value is $E(V-I) = 0.078$. We transformed this value using the relation $E(B-V) = 0.8 \cdot E(V-I)$, obtaining a final value of $E(B-V) = 0.062$.

## 3.2 Determination of the stellar parameters

The stellar parameters, such as the effective temperature, $T_{eff}$, the surface gravity, $\log g$, and the microturbulent velocity, $v_{turb}$, were determined using the Gaia and 2MASS photometric data.
The Python code that computed the parameters requires as input:

- The three Gaia magnitudes, G, BP, RP, with the respective errors, and the K magnitude with its error from the 2MASS catalogue.
- The value of the colour excess obtained from Skowron+21
- A generic value for the metallicity of [Fe/H]= $-0.5$ dex (consistent with the results in Van der Swaelmen et al., 2013). It is worth noting that the derived temperatures are poorly sensitive to the precise value of the adopted metallicities: a difference of 0.1 dex on [Fe/H] only affects the result on the temperature for $\sim 10$ K.
- A value for the stellar mass. According to Mucciarelli et al. (2023), we adopted a value of 1 $M_{\odot}$ for all the targets, representative of the typical stellar masses of RGB stars in intermediate age populations.
- A value for the distance modulus of the LMC. Here we adopted for all the stars a distance modulus of $\mu = 18.5$, assuming that the thickness of the LMC is negligible with respect to its distance.

The values of the effective temperatures for each star were computed using the colour - $T_{eff}$ transformations from Mucciarelli et al. (2021), which are based on the Gaia Data Release 3 (Gaia Collaboration et al., 2023) and 2MASS photometry (Skrutskie et al., 2006).
The program first of all corrects the magnitudes for extinction and applies the transformations for the six colour combinations $(BP-RP), (BP-G), (BP-K), (G-RP), (G-K)$, and $(RP-K)$.
Using the appropriate coefficients $b_0, ..., b_5$ from Mucciarelli et al. (2021) based on the specific de-reddened colour $C$ and the evolutionary stage of the star (giants in this case), $T_{eff}$ is determined as:

$$\theta = b_0 + b_1 C + b_2 C^2 + b_3[\mathrm{Fe/H}] + b_4[\mathrm{Fe/H}]^2 + b_5[\mathrm{Fe/H}]C \tag{3.1}$$

$$T_{eff} = 5040/\theta \tag{3.2}$$

Then, the luminosity of each star $L$ is computed from the bolometric magnitude using the distance modulus provided as input. This allows to estimate the radius of the star $R$ using the Stefan-Boltzmann law ($\sigma = 5.67 \cdot 10^{-5}\ erg\ cm^{-2}\ s^{-1}\ K^{-4}$):

$$L = 4\pi R^2 \sigma T_{eff}^4 \tag{3.3}$$

Finally, the surface gravity is estimated from the physical definition, using the radius just computed, the stellar mass $M$ provided as input and the gravitational constant $G = 6.67 \cdot 10^{-8}\ g^{-1}\ cm^3\ s^{-2}$:

$$g = \frac{GM}{R^2} \tag{3.4}$$

In this study, we decided to use for all the targets the temperatures derived from the $G - K$ colours (and the corresponding $\log g$) for consistency with the analysis by Anoardo et al. (2026), in order to avoid possible systematics due to the use of different colours.

The microturbulent velocity is an important value that parametrizes the effect of convective motions in the stellar atmospheres. As a matter of fact, convective cells can rise toward the surface of the stellar atmosphere, or drop towards the inner layers, producing an additional broadening in the line profile.
The standard 1-dimensional model atmospheres (that describe any physical quantity as a function of the optical depths) are not able to properly and fully describe the convection. Therefore, the use of these models fails to reproduce the line broadening of the strong and saturated lines (that are the most sensitive to the convective motions). On the other hand, lines on the linear part of the curve of growth are not affected.
In order to overcome this limitation of the 1-dimensional model atmospheres, a corrective parameter, named microturbulent velocity, is adopted in the line profile computation.
Usually, this parameter is constrained by forcing weak and strong Fe lines to have the same abundances. However, this procedure would need a large amount of Fe lines, covering a wide range of line strengths. In the case of the FLAMES spectra that we have in hand, the number of Fe lines is too small to properly constrain this parameter, and we rely on the relation by Mucciarelli & Bonifacio (2020) that calibrates $v_{turb}$ as a function of $\log g$.
Since the linear relation for $v_{turb}$ is different for [Fe/H]$< -2.1$ dex and [Fe/H]$> -2.1$ dex, the minimum value of metallicity in the data from Van der Swaelmen et al. (2013) is identified. We found a minimum value of [Fe/H]$= -1.69$ dex among the bar stars, ensuring the use of the appropriate linear relation:

$$v_{turb} = (-0.37 \pm 0.03) \cdot \log g \ + \ (2.08 \pm 0.04) \quad (\sigma = 0.13) \tag{3.5}$$

Using the value of $\log g$ obtained in the previous step, from the colour $G - K$, the corresponding $v_{turb}$ is computed for each star using the formula 3.5.
Results obtained for the stellar parameters are compared with the counterpart from Van der Swaelmen et al. (2013) in Fig. 3.1.
Finally, the results for $T_{eff}$ and $\log g$ can be displayed in a Kiel diagram in Fig. 3.2. The values of $T_{eff}$ vary between 3693 K and 4971 K, while the values for $\log g$ range between 0.81 dex and 1.6 dex, which is consistent with what is expected for red giant stars.

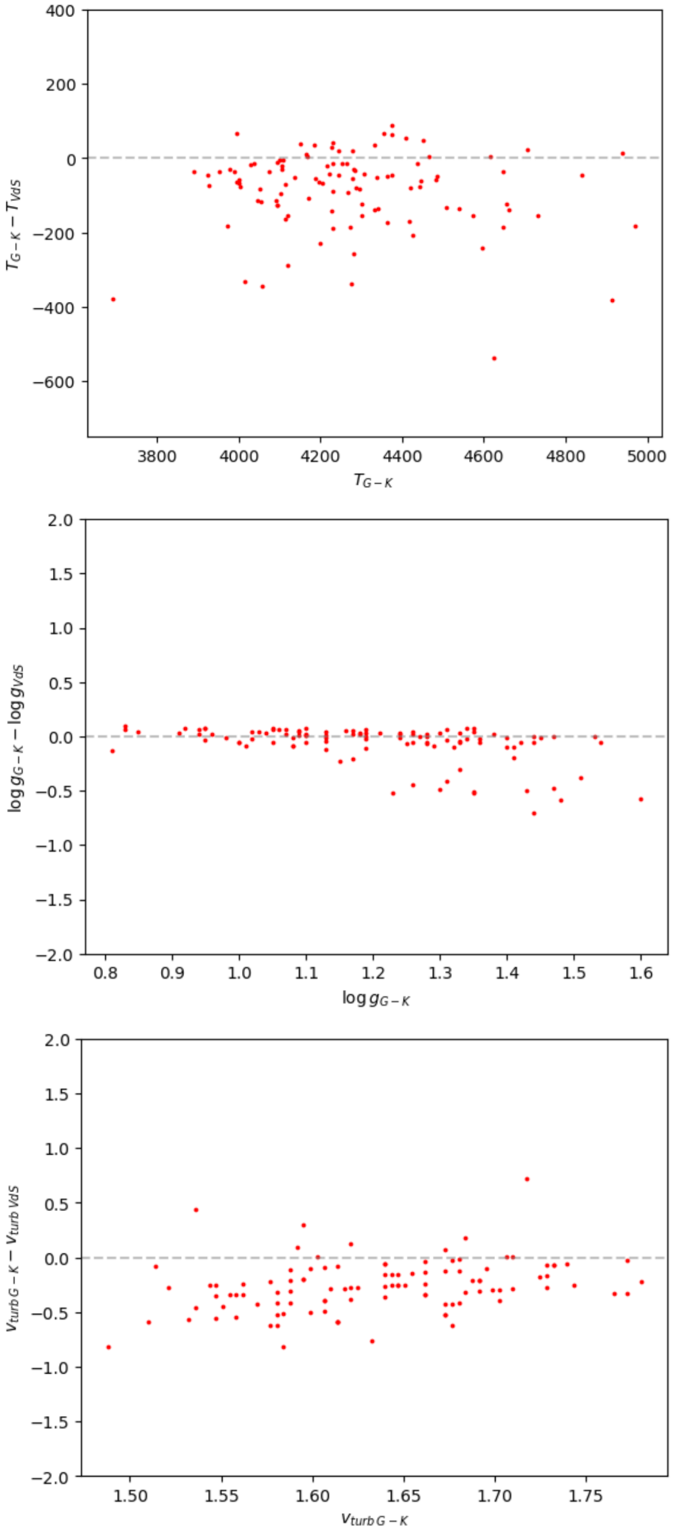


**Figure 3.1:** Comparison of the stellar parameters. In order, the top, middle and bottom panels show the difference between the effective temperature, the surface gravity and the microturbulent velocity obtained from the $G - K$ colour in this work, and the values from Van der Swaelmen et al. (2013).

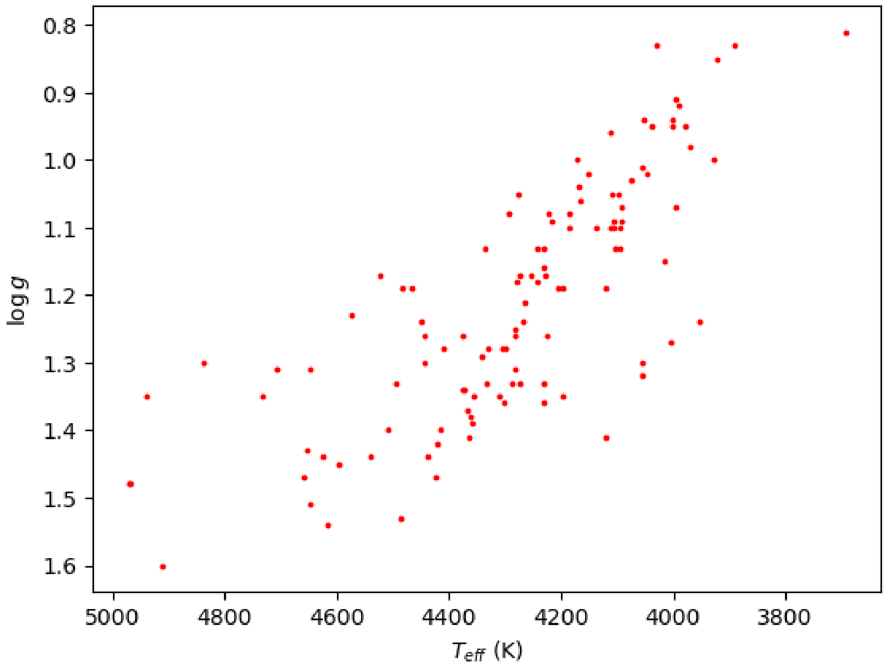


**Figure 3.2:** Kiel diagram showing the position of the target stars in the $T_{eff} - \log g$ plane.

## 3.3 Preparation for the analysis

In this section, we explain the steps needed to prepare the spectra for the chemical analysis: normalization, correction for radial velocity, estimate of the SNR and identification of the lines for the chemical analysis.

### 3.3.1 Radial velocity correction and normalization

The radial velocity correction is performed to measure the Doppler shift caused by the component of the star velocity along the line of sight.
The correction is carried out using the program `slab` (developed at the Department of Physics & Astronomy, University of Bologna) containing the command `rvlist`. Providing a file listing the spectra that need to be corrected, and a template spectrum of known radial velocity, it calculates the cross-correlation function (CCF). The CCF describes the correlation probability between the observed spectrum (shifted one pixel at a time) and the template spectrum of known radial velocity (see Fig. 3.3).
In order to define the radial velocity, the main peak of the CCF is fitted with a gaussian profile and the centre of the best-fit is assumed as the best-fit radial velocity.

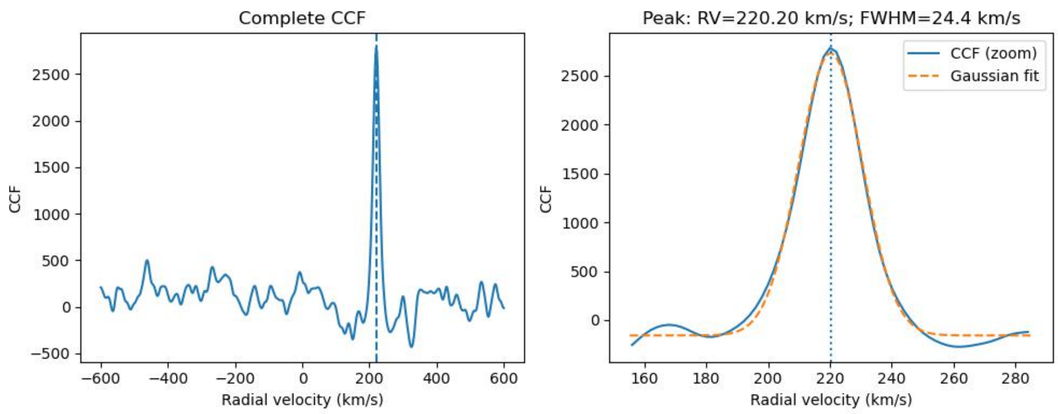


**Figure 3.3:** Cross-correlation function computed for the spectroscopic target 05223895-6945007. The left panel shows the entire cross-correlation function, while the right panel shows only the region around the main peak with the best-fit Gaussian profile.

As template spectra, we adopted synthetic spectra calculated with the code `k2` (Mucciarelli et al. in preparation). Because the target stars have similar parameters, we used a single template spectrum for each setup, which was computed adopting the average stellar parameters of the bar stars ($T_{eff} = 4283\ K$, $\log g = 1.21$ dex and $v_{turb} = 1.63\ km\,s^{-1}$) and representative values of $-0.5$ dex for the metallicity and [$\alpha$/Fe]= +0.4 dex. It is worth noting that the precise value of [$\alpha$/Fe] used to compute the synthetic spectra has a negligible effect on the measured radial velocity. The output of `synthe` consists of three files, a non-broadened synthetic spectrum, in which absorption lines only show the intrinsic broadening and the effect of the stellar atmosphere, a synthetic spectrum with the additional contribution of the instrumental broadening, and table including the lines used in the synthetic spectrum.

The normalization of the spectra was performed with the command `splinelist` in the program `slab`. The program performs a fitting of the continuum using the spline method and avoiding the pixels relative to spectral lines.
Providing the .fits file of the spectra and choosing $k = 3$, $\sigma = 2$, respectively the degree of the spline and the number of standard deviations to reject points of line/noise, the program provides as output the normalized spectra.
An example of this procedure is shown in Fig. 3.4.

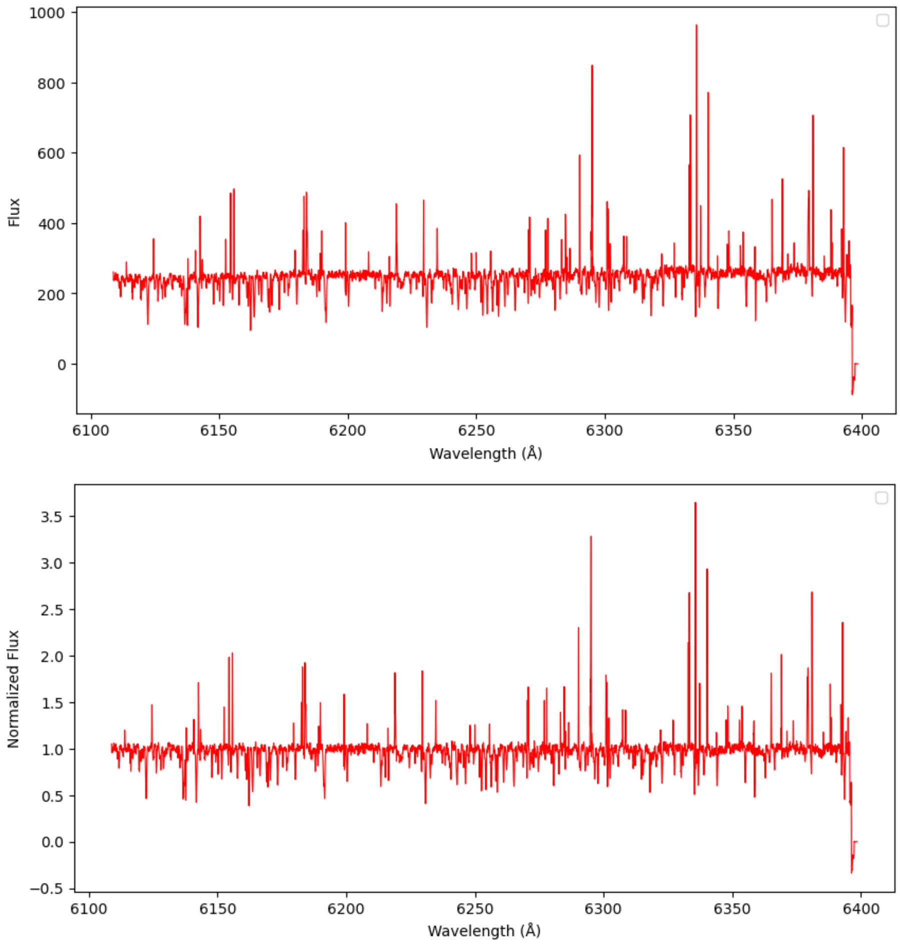


**Figure 3.4:** In the top panel, the observed spectrum of star 05252899-6939078 in the HR13 setup. In the bottom panel, the result of the normalization procedure.

### 3.3.2 Estimate of the SNR and broadening of lines due to external processes

As explained below, in order to select the lines for the chemical analysis, it is necessary to know the SNR of the spectra. The estimate of the SNR for each spectrum is performed using `slab` and the command `snr`.
This command allows to select interactively continuum regions without lines. We selected spectral regions of 1-2 Å of amplitude, calculating the SNR as the median value of the flux, normalized to the flux standard deviation.
First of all, a brighter and a fainter star were considered to investigate whether the SNR is constant across different wavelengths. In each setup, three values of the SNR were determined at the beginning and at the end of the spectrum. As a result, SNR is seen to vary only a little with wavelength in the setups HR11 and HR13, while it is seen to change more in HR14A, probably due to the different curve of efficiency of each setup.
Finally, for each star and setup we estimated the SNR across the corresponding spectral range.

Another piece of information useful to calculate appropriate synthetic spectra for the line selection and for the subsequent chemical analysis, is the observed broadening of the lines. The observed broadening is the convolution of different effects, including the intrinsic broadening of the lines, the instrumental profile and additional broadening arising mainly from convective motions in the stellar atmospheres.
To estimate the broadening of the lines, the option `fitline` in `slab` was used, allowing to perform the gaussian fitting of a spectral line. Providing the observed spectrum, and the instrumental resolution as an initial guess, the FWHM of the best-fit model of a certain line is determined.
For an intermediate brightness star, we measured the FWHM of 15-20 spectral lines. The median value reported in table 3.1 was chosen as representative for each setup.

| | HR11 | HR13 | HR14A |
|---|---|---|---|
| FWHM (Å) | 0.313 | 0.370 | 0.490 |

**Table 3.1:** Median values for the measured FWHM for each setup.

Lastly, given the observed FWHM in table 3.1, the instrumental resolution in table 2.1, and assuming a contribution from the intrinsic broadening of 0.1 Å, the value of the broadening from further effects can be determined as:

$$FWHM_{extra} = \sqrt{FWHM_{obs}^2 - 0.1^2} \tag{3.6}$$

At this point, the corresponding resolution, which includes the effect of the instrumental and the extra broadening, is computed as follows:

$$R_{in+extra} = \lambda_{central}/FWHM_{extra}$$

Results are listed in table 3.2.

| | $FWHM_{obs}$ (Å) | $FWHM_{extra}$ (Å) | $\lambda_{central}$ (Å) | $R_{in+extra}$ |
|---|---|---|---|---|
| HR11 | 0.313 | 0.300 | 5718.5 | 19280 |
| HR13 | 0.370 | 0.384 | 6262.5 | 16320 |
| HR14A | 0.490 | 0.479 | 6504.5 | 13560 |

**Table 3.2:** Results for the different contributions to the broadening of lines and resolution in the three setups.

## 3.3.3 Identification of the lines in the spectra and line selection

The last step before the chemical analysis is the line selection. Our aim is to select atomic transitions for the elements of interest, that are possibly unblended and as clearly detectable as possible, according to the observed SNR of our spectra.
We used the code `k2` to select the lines according to the following procedure.
First of all, synthetic spectra representative of the observed targets in terms of stellar parameters and metallicities were calculated using the code `synthe` (Kurucz, 2005). For the computations, the appropriate resolution for each GIRAFFE setup of our dataset was provided. Also, at this step, the [Eu/Fe] was increased by +0.7 dex with the goal of observing the Eu line at 6645 Å in the synthetic spectra.
Then, all the available features (that could be isolated or blended lines) in a synthetic spectrum were identified as local minima using the option `sline2` in the `k2` code. The features that are weaker than a given threshold (provided as input parameter according to the measured SNR of the spectra) are automatically excluded as considered not detectable within the observed noise.
For each minimum, the strongest transition available within the line profile is identified. The code also computes for each transition the variation in abundance arising when we consider the corresponding feature unblended, to quantify the effect of possible blending. The graphical output of `sline2` is shown in Fig. 3.5.

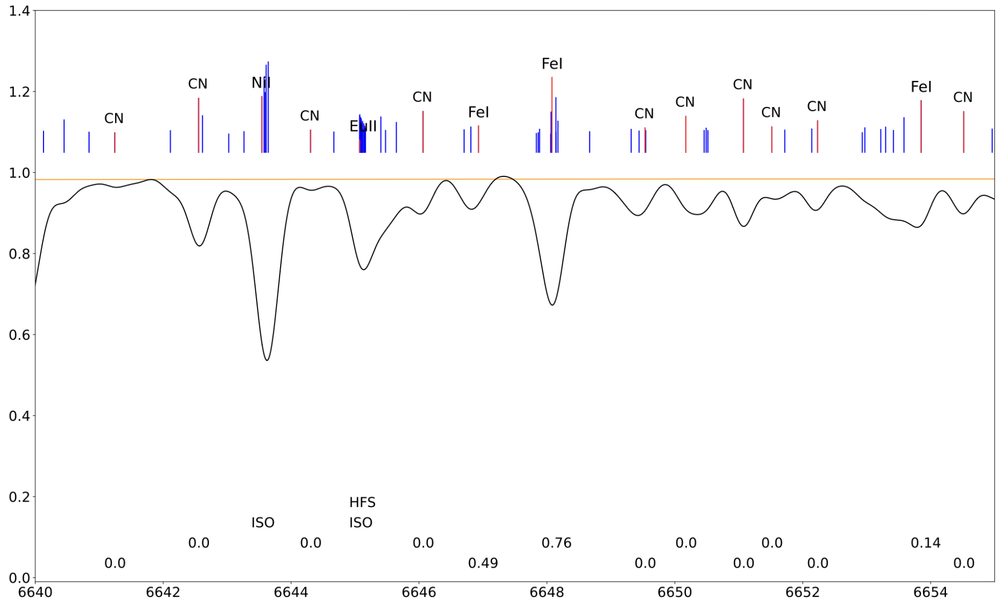


**Figure 3.5:** Example of the output of `sline2` for the synthetic spectrum covering the wavelength range of the setup HR14A, zoomed on the Eu line at 6645 Å.

Once the absorption lines in the three synthetic spectra were identified, we selected the lines suitable for the chemical analysis. Weak lines should be avoided due to their low SNR, meaning that any small fluctuation can affect the result on the element abundance. On the other hand, excessively strong and saturated lines should be excluded because their equivalent width is no longer sensitive to small

abundance variations, providing unreliable results. Finally, lines characterized by a value of $deltaAbu > 0.05$, describing a high level of contamination from unresolved features, were excluded.
The ideal lines to choose are of moderate strength, with clean and unblended profiles. According to these considerations, we obtained a linelist including:

- Around 50 lines of Fe I
- The Mg I line at 5711 Å
- The Ba II line at 6496.9 Å
- The Eu II line at 6645.1 Å

## 3.4 Chemical analysis with `salvador`

The chemical analysis was performed with the program `salvador` (Alvarez Garay et al. in preparation). Chemical abundances are derived with a $\chi^2$ minimization between lines in the observed spectra and lines from synthetic spectra at different abundances. The synthetic spectrum with the minimum $\chi^2$ is identified and used to obtain the final estimate of the abundance.
First of all, the program requires the observed normalized spectra, in this case, already corrected for the radial velocity.
Then the atmospheric parameters of each star need to be provided, as they are used when the program `k2` is called to compute the synthetic spectra at different abundances.
The observed stars are all located in the bright portion of the RGB, brighter than the RGB Bump. Therefore these stars have already experienced the mixing episode at the luminosity level of the RGB Bump. The main effect of this mixing is the creation of the C-N anti-correlation, in which C is decreased and N is increased. For this reason, during the computations of the synthetic spectra, we assumed that the abundances of C and N were modified by -0.5 and +0.5 dex respectively.
Other information provided to the program includes the list of atomic transitions to be analysed selected in the previous step, with the relative wavelength, and the resolution computed in section 3.3.2 to broaden the lines in the synthetic spectra.
The output is a .pdf file provided for each spectrum (as shown in Fig. 3.6) displaying each analysed line with the best fit model over-imposed. Also, a .fit file reporting the estimate of the abundance for each line is created.

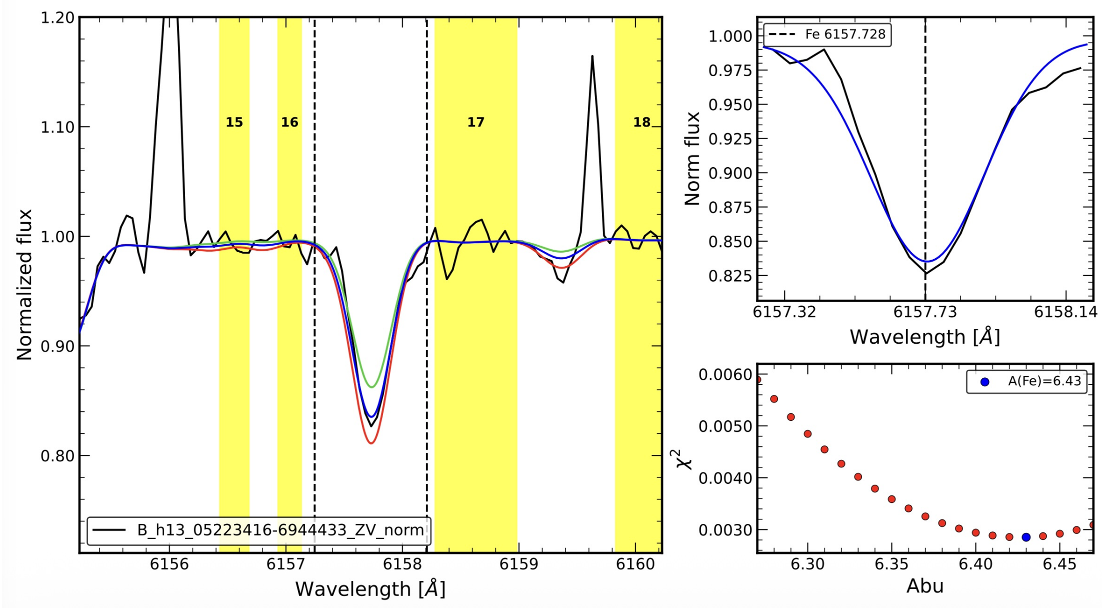
B_h13_05223416-6944433_ZV_norm
Normalized flux
Wavelength [Å]
15
16
17
18
Fe 6157.728
Norm flux
Wavelength [Å]
A(Fe)=6.43
$\chi^2$
Abu

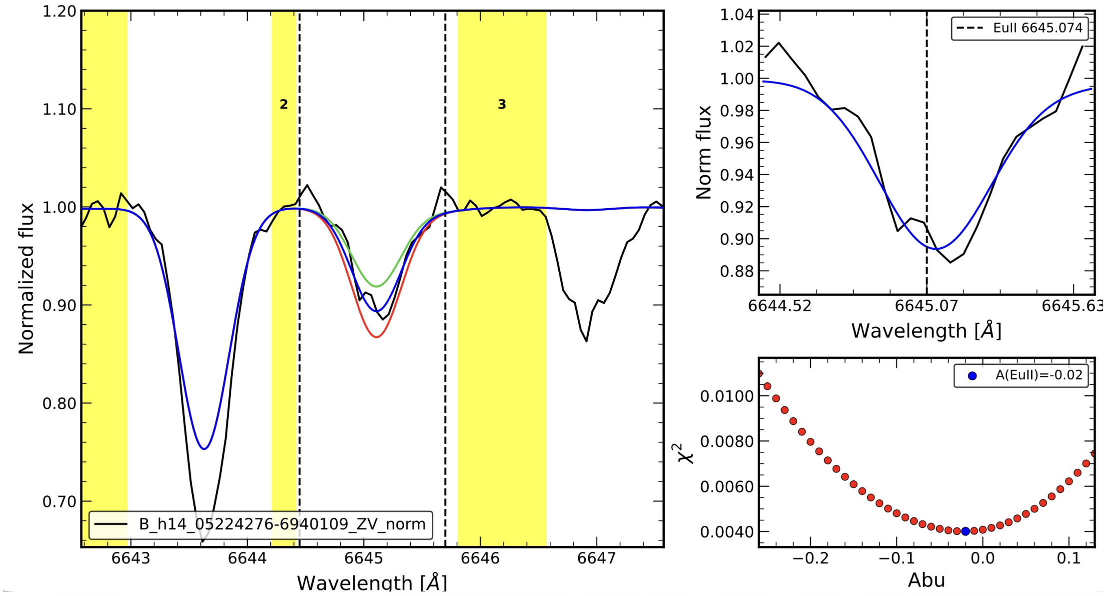
B_h14_05224276-6940109_ZV_norm
Normalized flux
Wavelength [Å]
2
3
EuII 6645.074
Norm flux
Wavelength [Å]
A(EuII)=-0.02
$\chi^2$
Abu

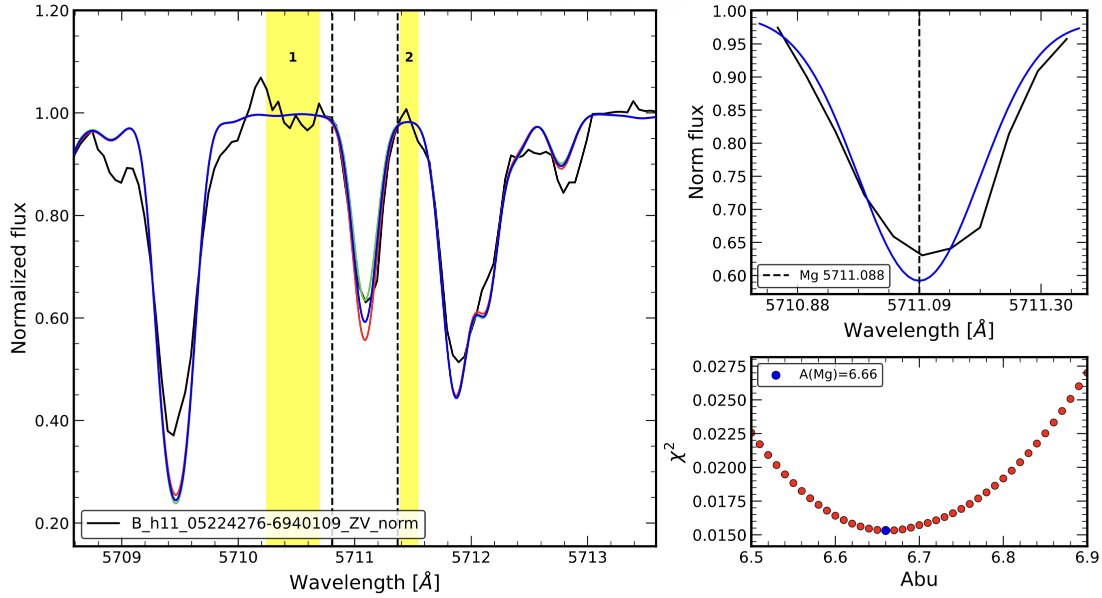
B_h11_05224276-6940109_ZV_norm
Normalized flux
Wavelength [Å]
1
2
Mg 5711.088
Norm flux
Wavelength [Å]
A(Mg)=6.66
$\chi^2$
Abu

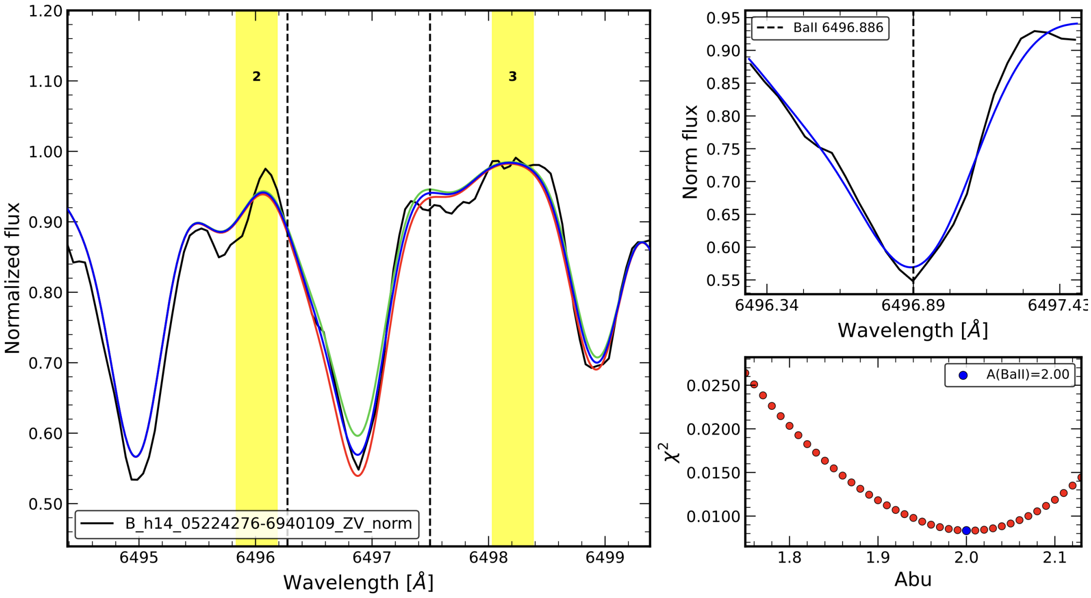


**Figure 3.6:** Graphical outputs from `salvador`. In the top panel the fitting of the Fe line at 6157.7 Å for star 05223316-6951389 is shown. In the second, third and fourth panels, the fitting of the Eu line at 6645 Å, Mg line at 5711 Å, and Ba line at 6496.9 Å for star 05224276-6940109 are represented. In each panel, the pictures on the left show a zoom of the observed spectrum of the star (black line) centered on the analysed line (between the vertical dashed lines). The yellow windows are continuum regions that were used to guide the normalization. The red, blue and green lines represent three models at different abundances. The blue one, being the best-fit, is also displayed on the top right of each panel. On the bottom right of each panel, the $\chi^2$-minimization is shown as a function of the abundance.

## 3.5 Treatment of uncertainties

Uncertainties on the chemical abundances are determined by two sources of errors. The first kind of uncertainty is the one arising from the stellar parameters that were used to compute the model atmospheres ($T_{eff}$, $\log g$, $v_{turb}$).
The second kind of uncertainty is generated in the line-fitting procedure during the chemical analysis.
Both sources of uncertainties are handled by the program `salvador` as follows:

- Uncertainties from the atmospheric parameters are estimated repeating the chemical analysis varying each time a specific parameter. Considering typical errors of $\pm 60\ K$ for $T_{eff}$, $\pm 0.1$ dex for $\log g$ and $\pm 0.2\ km\ s^{-1}$ for $v_{turb}$, at each iteration one parameter is varied, while the others are kept constant.

- Uncertainties arising from the fitting procedure of $N_X > 1$ lines of a certain element X are determined as $\sigma_X / N_X$, the ratio between the standard deviation of the mean abundance and the number of lines. On the other hand, if only one line for the specific element is available, the uncertainty is determined as the error arising from 200 Monte Carlo simulations.

The final errors for [Fe/H] and [X/Fe] are computed summing in quadrature the different contributions as:

$$\sigma_{\text{[Fe/H]}} = \sqrt{\frac{\sigma^2_{Fe}}{N_{Fe}} + \left(\delta^{T_{eff}}_{Fe}\right)^2 + \left(\delta^{\log g}_{Fe}\right)^2 + (\delta^{v_{turb}}_{Fe})^2} \tag{3.7}$$

$$\sigma_{\text{[X/Fe]}} = \sqrt{\frac{\sigma^2_{Fe}}{N_{Fe}} + \frac{\sigma^2_{X}}{N_{X}} + \left(\delta^{T_{eff}}_{X} - \delta^{T_{eff}}_{Fe}\right)^2 + \left(\delta^{\log g}_{X} - \delta^{\log g}_{Fe}\right)^2 + (\delta^{v_{turb}}_{X} - \delta^{v_{turb}}_{Fe})^2} \tag{3.8}$$

where $\delta^i_{Fe}$ and $\delta^i_X$ are the are the abundance variations obtained modifying the atmospheric parameters.
For abundances such as [X/Y] = [X/Fe] − [Y/Fe], the final error is determined as:

$$\sigma_{\text{[X/Y]}} = \sqrt{\sigma^2_{\text{[X/Fe]}} + \sigma^2_{\text{[Y/Fe]}}} \tag{3.9}$$

# Chapter 4

# Results

## 4.1 [Mg/Fe] abundances

The [$\alpha$/Fe] abundance ratios are the most widely used diagnostics to describe the chemical enrichment of a galaxy.
While $\alpha-$elements are mainly produced by CC-SNe on short timescales, Fe is produced from SNe Ia on significantly longer timescales. Because of this time delay between the two classes of SNe, the [$\alpha$/Fe] abundance ratios serve as tracers of the relative contributions from the different SNe to the chemical enrichment of the ISM (Oemler & Tinsley, 1979; Matteucci & Greggio, 1986).
Differently from other $\alpha-$elements which can be synthetized also in SNe Ia, Mg is produced almost exclusively by the $\alpha-$capture process in very massive stars exploding as CC-SNe (Kobayashi et al., 2020). Therefore, the behaviour of [Mg/Fe] as a function of [Fe/H] is the preferred diagnostic to provide information about the relative efficiency of CC-SNe versus SNe Ia. As a matter of fact, a clear decreasing trend in the pattern of [Mg/Fe] versus [Fe/H] is expected starting from the first SNe Ia explosions, causing a decrease in the relative abundance of $\alpha-$elements.
Figure 4.1 shows the [Mg/Fe] abundances as a function of [Fe/H] in the LMC. As the metallicity increases, LMC stars show a depletion of [Mg/Fe] with respect to the solar value, sign that these stars were born in a gas that had already been polluted by SNe Ia. Although the ages of individual stars are not known, based on theoretical age-metallicity relations (see e.g. Pagel & Tautvaisiene, 1998) these stars should be around 5-6 Gyrs old, ensuring that SNe Ia had the time to enrich the ISM.
Figure 4.2 compares the behaviour of [Mg/Fe] as a function of [Fe/H] for our sample of LMC stars with the SMC stars from Anoardo et al. (2026) and the Milky Way stars (data from the SAGA database, Suda et al., 2008).
In order to highlight the behaviour of each galaxy, we plotted the median trend for each sample, calculated using a Gaussian KDE (Kernel Density Estimation) regression.
The median trend of [Mg/Fe] as a function of [Fe/H] in the LMC is clearly deficient with respect to Milky Way stars of the same [Fe/H]. Also, the metal-poorer $\alpha-$knee in the LMC reflects the lower star formation efficiency of the galaxy with respect to the Milky Way, resulting in a slower enrichment before the first SNe Ia explosions.

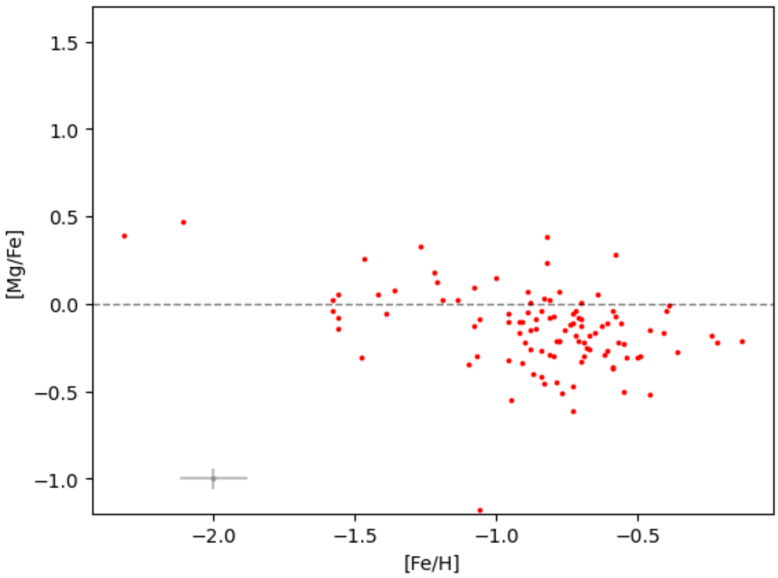


**Figure 4.1:** [Mg/Fe] abundances as a function of [Fe/H] for the LMC stars. The gray dashed line represents the solar value of [Mg/Fe]. The errorbar shown in the lower left corner is representative of the typical uncertainty.

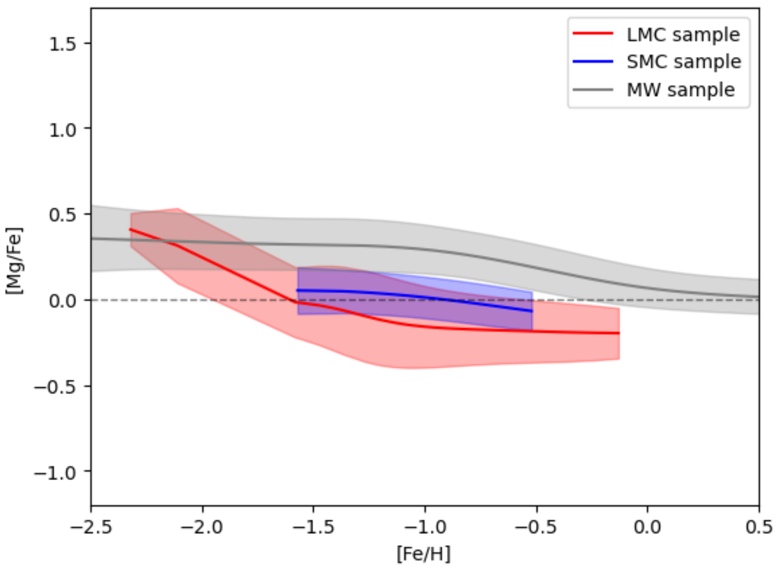


**Figure 4.2:** Median trends of [Mg/Fe] against [Fe/H] for LMC stars in red (this work), SMC stars in blue (Anoardo et al., 2026) and Milky Way data in gray (Suda et al., 2008). The solid lines are non-parametric Gaussian KDE (Kernel Density Estimation) regressions, while the shaded areas represent the $1\sigma$ confidence intervals of the regressions. The gray dashed line represents the solar value of [Mg/Fe].

## 4.2 [Eu/Fe] abundances

The results for the Eu abundances of the LMC stars are represented in Fig. 4.3 which shows [Eu/Fe] as a function of [Fe/H].
Only 9 stars of the sample have [Fe/H]$< -1.25$ dex. Despite the small statistics, which do not allow firm conclusions to be drawn, these stars are clearly enhanced, indicating a large efficiency of the r-process at low metallicities (corresponding to the first few Gyrs of life of the LMC).
At higher metallicities, where we have the bulk of the stars of our sample, [Eu/Fe] exhibits a clear decreasing trend as a function of [Fe/H], approaching solar-scaled values at the highest metallicities. The bulk of the sample has [Fe/H]$\sim -0.75$ dex, with [Eu/Fe] around +0.5 dex and +0.6 dex, indicating a strong efficiency of the r-process.
A comparison between the spectroscopic targets from the LMC, results for the SMC (Anoardo et al., 2026) and data for the Milky Way from the SAGA database (Suda et al., 2008) is shown in Fig. 4.4.
This result confirms that in the metallicity range covered by the three galaxies ($-1.5 \lesssim$[Fe/H]$\lesssim -0.5$ dex) LMC stars are indeed enriched in r-process elements with respect to the Milky Way, with values similar to those of the SMC. However, while the LMC median trend is higher, it is still within the $1\sigma$ confidence region of the Milky Way. This implies that despite the slight enhancement, at first approximation, the [Eu/Fe] remains compatible with the Galaxy.
Finally, a decreasing trend in [Eu/Fe] can also be observed in all galaxies starting from [Fe/H]$\gtrsim -1.5$ dex. The reason for this decline is the onset of SNe Ia which inject Fe in the ISM but do not produce Eu.

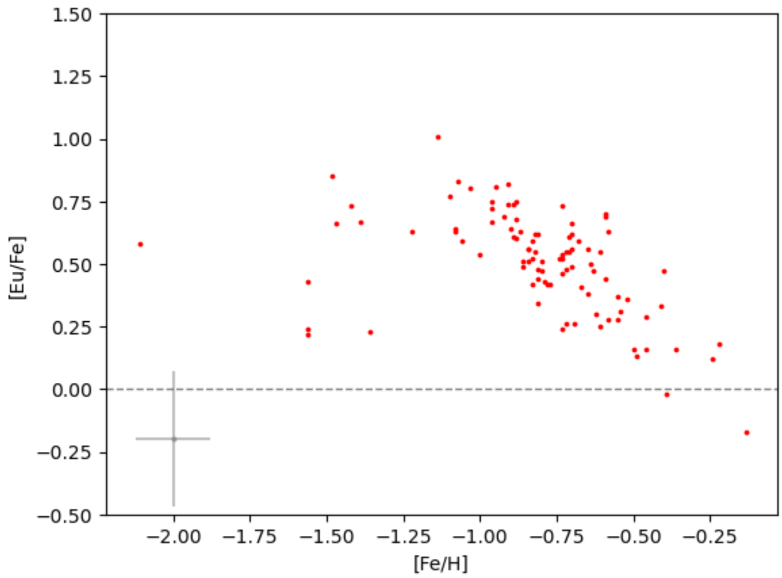


**Figure 4.3:** [Eu/Fe] abundances as a function of [Fe/H] for the LMC stars. The gray dashed line represents the solar value of [Eu/Fe]. The errorbar shown in the lower left corner is representative of the typical uncertainty.

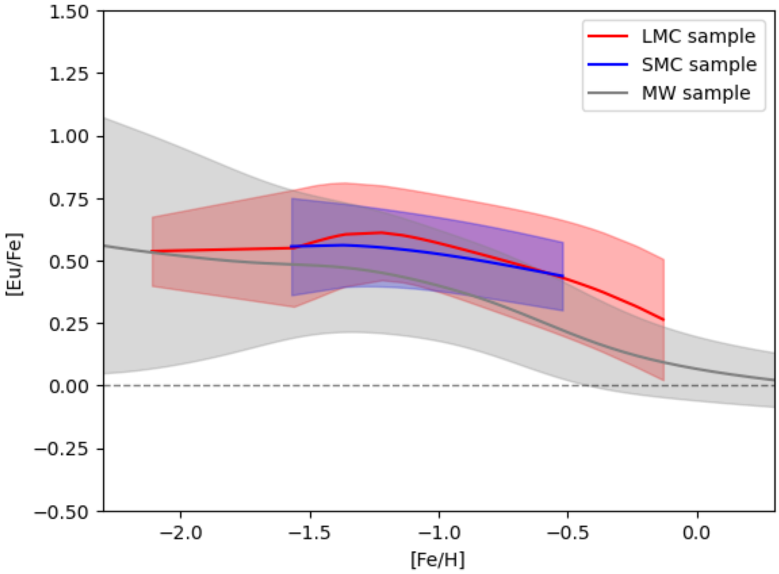


**Figure 4.4:** Median trends for [Eu/Fe] against [Fe/H] for LMC stars in red (this work), SMC stars in blue (Anoardo et al., 2026) and Milky Way data in gray(Suda et al., 2008). The solid lines are non-parametric Gaussian KDE regressions, while the shaded areas represent the 1$\sigma$ confidence intervals of the regressions. The gray dashed line represents the solar value of [Eu/Fe].

## 4.3 [Ba/Fe] abundances

Results on the [Ba/Fe] abundance ratios in the LMC are reported in Fig. 4.5.
The overall high values of [Ba/Fe] around $\sim +0.6$ dex for the bulk of the stars indicate that Ba production is very efficient in the galaxy.
Moreover, a clear increasing trend with [Fe/H] is observed, reaching values of [Ba/Fe] $\sim +0.8$ dex at the highest metallicities of our sample. Barium is at first produced by the r-process, which provides only a small contribution at the lower metallicities. At later times, s-process nucleosynthesis in AGB stars dominates the production of Ba, causing the observed increase.
Comparing results, the values of [Ba/Fe] in the LMC are found to be more increased than those of the SMC, while both are systematically higher than those of the Milky Way (Fig. 4.6). This observation can be explained by the fact that the production of Ba from AGB stars is stronger for metal-poorer stars, which is a typical scenario for dSphs.

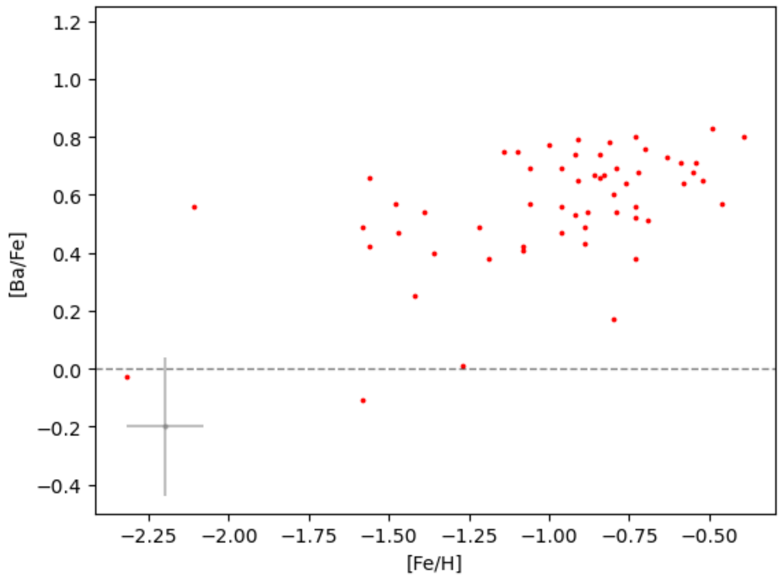


**Figure 4.5:** [Ba/Fe] abundances as a function of [Fe/H] for the LMC stars. The gray dashed line represents the solar value of [Ba/Fe]. The errorbar shown in the lower left corner is representative of the typical uncertainty.

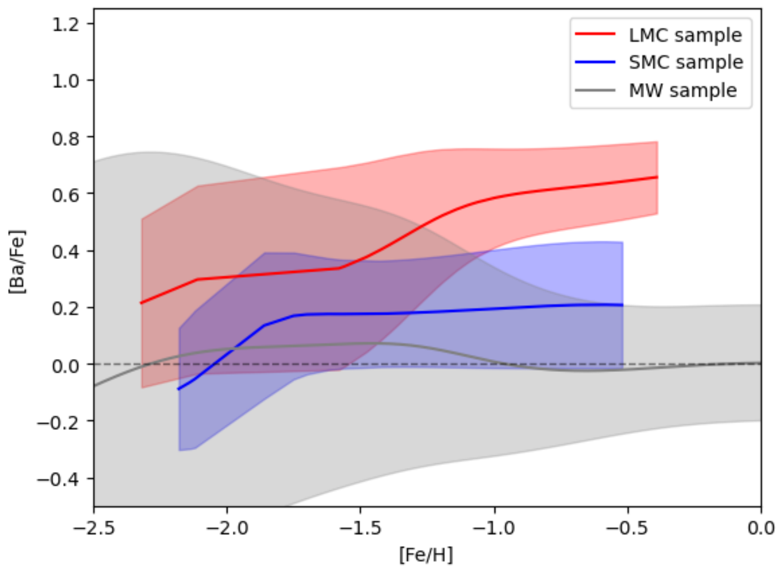


**Figure 4.6:** Median trends for [Ba/Fe] against [Fe/H] for LMC stars in red (this work), SMC stars in blue (Anoardo et al., 2026) and Milky Way data in gray (Suda et al., 2008). The solid lines are non-parametric Gaussian KDE regressions, while the shaded areas represent the $1\sigma$ confidence intervals of the regressions. The gray dashed line represents the solar value of [Ba/Fe].

## 4.4 [Eu/Mg] abundances

The results for the abundance ratio [Eu/Mg] are particularly interesting as they allow to quantify the relative efficiencies of the r-process and the $\alpha-$capture.
Figure 4.7 shows the [Eu/Mg] abundances as a function of [Fe/H]. Despite a significant star-to-star scatter ($\sigma = 0.38$) the high values of [Eu/Mg] around +0.7 dex and +0.8 dex display a clear enhancement with respect to solar values.
A comparison with the SMC results from Anoardo et al. (2026) and the Milky Way data from the SAGA database (Suda et al., 2008) is helpful to better understand the situation (Fig. 4.8).
For $-1.5 \lesssim$[Fe/H]$\lesssim -0.5$ dex, both the LMC and SMC show enhanced values of [Eu/Mg], systematically higher than those from the Milky Way, with an off-set of $\sim 0.4$ dex. This proves a stronger enrichment in r-elements with respect to $\alpha-$elements in the Magellanic Clouds.
As explained in section 1.2, Eu can be produced by the r-process mainly in two possible environments, a prompt source (represented by rare CC-SNe) and a delayed one (represented by NS mergers). Eventhough we still lack constraints on these sources and their relative efficiencies, we expect Eu and Mg to trace one another due to the different timescales of the respective process. Also, due to the rarity of the r-process sites, we expect a minor contribution to Eu with respect to Mg.
Chemical evolution models on the enrichment of r-process elements that well reproduce the observations in the Milky Way are found to underestimate [Eu/Fe] and [Eu/Mg] abundance ratios when applied to dSphs and the SMC (Palla et al., 2025, 2026). This indicates the need of an increased production of r-process in these dwarf galaxies, possibly from an additional source at low metallicities.
Based on these results for the LMC, the considerations on chemical enrichment models applied to other Local Group galaxies can be qualitatively extended also to the LMC.
Finally, the distinct trends of [Eu/Mg] in the Magellanic Clouds and the Milky Way, result of a slight enhancement in [Eu/Fe] and depletion of [Mg/Fe] with respect to the Galaxy, support the idea to use this abundance ratio as a tool for chemical tagging, to distinguish between stars that formed in situ, and stars that were accreted.

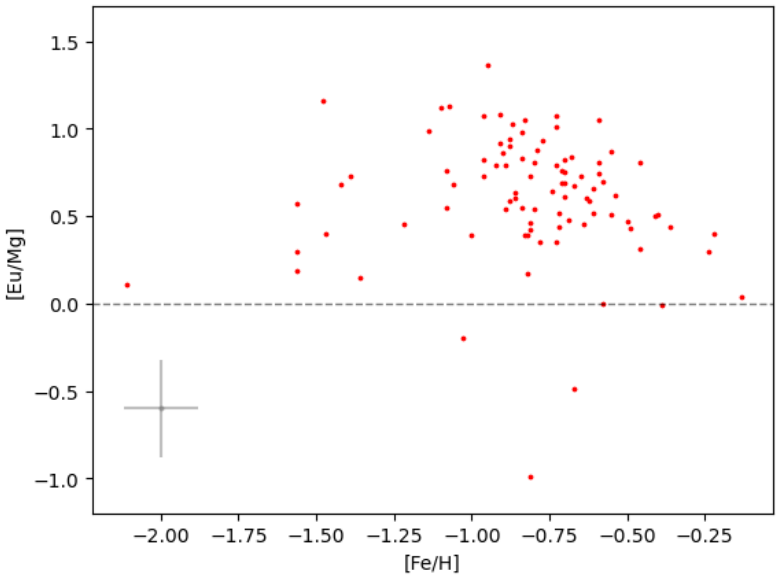


**Figure 4.7:** [Eu/Mg] abundances as a function of [Fe/H] for the LMC stars. The gray dashed line represents the solar value of [Eu/Mg]. The errorbar shown in the lower left corner is representative of the typical uncertainty.

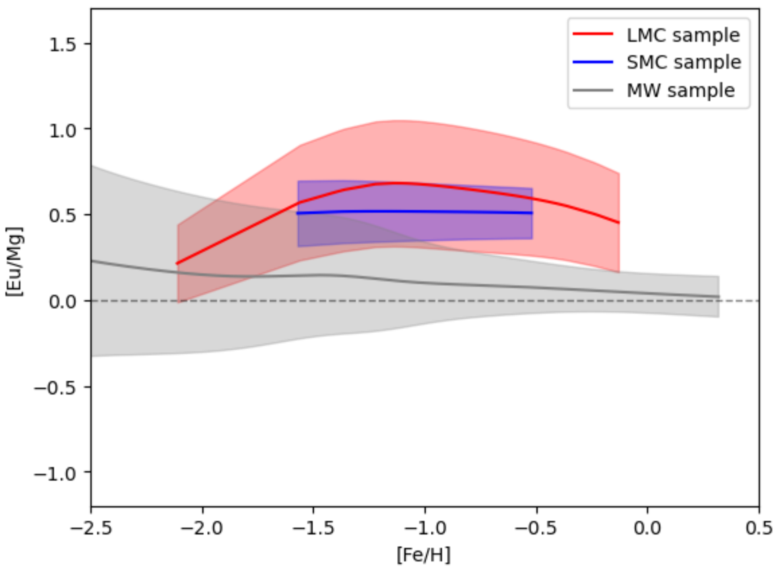


**Figure 4.8:** Median trends for [Eu/Mg] against [Fe/H] for LMC stars in red (this work), SMC stars in blue (Anoardo et al., 2026) and Milky Way data in gray (Suda et al., 2008). The solid lines are non-parametric Gaussian KDE regressions, while the shaded areas represent the $1\sigma$ confidence intervals of the regressions. The gray dashed line represents the solar value of [Eu/Mg].

## 4.5 [Ba/Eu] abundances

The abundance ratio [Ba/Eu] is an indicator of the relative contribution between the s-process (traced by Ba) and the r-process (traced by Eu).
Figure 4.9 displays [Ba/Eu] abundances as a function of [Fe/H]. The values increase with the metallicity of the stars, starting from [Ba/Eu]$\sim -0.3$ dex and reaching values around $\sim +0.7$ dex. This is consistent with the progressive enrichment of the ISM from the s-process in AGB stars and with the dominance of the slow neutron-capture process with respect to the rapid one in the LMC.
Finally, we compared the median trends of the abundance ratios of [Ba/Eu] in the LMC, Milky Way and SMC in Fig. 4.10.
Since the LMC exhibits the highest [Ba/Eu] values, we can conclude that AGB stars contributed more strongly to the s-process enrichment in this galaxy than in the Milky Way or the SMC.

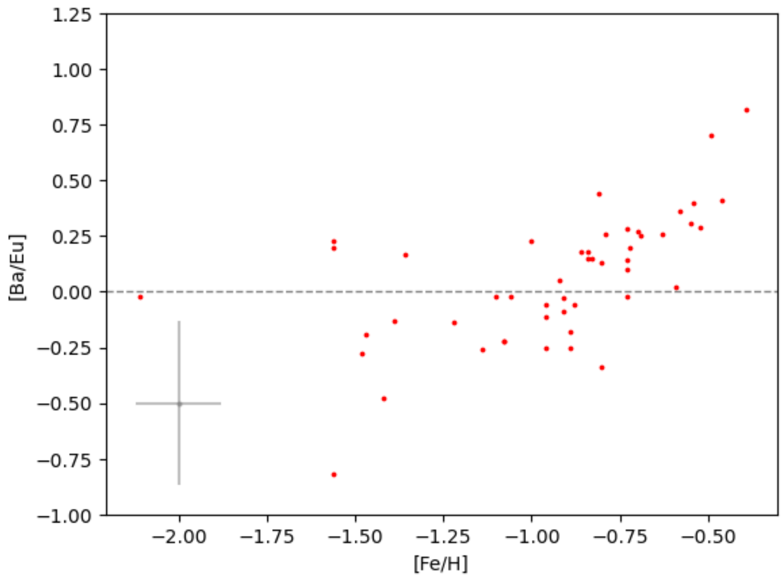


**Figure 4.9:** [Ba/Eu] abundances as a function of [Fe/H] for the LMC stars. The gray dashed line represents the solar value of [Ba/Eu]. The errorbar shown in the lower left corner is representative of the typical uncertainty.

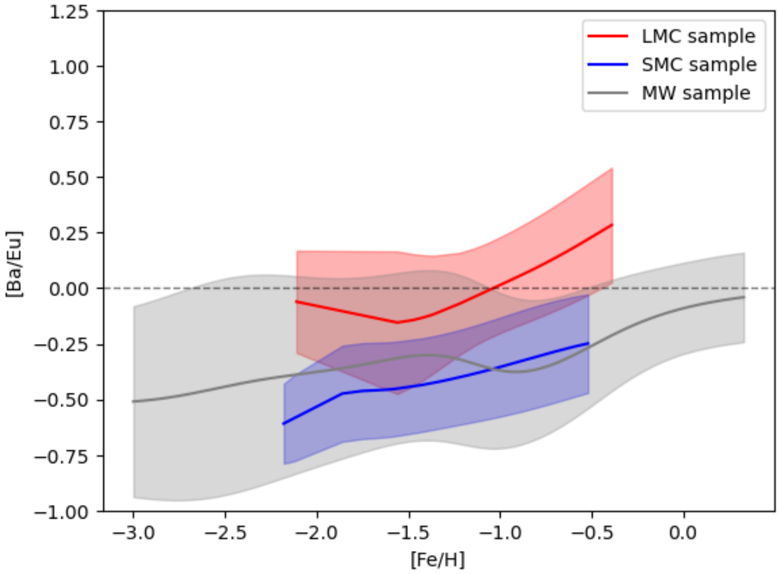


**Figure 4.10:** Median trends for [Ba/Eu] against [Fe/H] for LMC stars in red (this work), SMC stars in blue (Anoardo et al., 2026) and Milky Way data in gray (Suda et al., 2008). The solid lines are non-parametric Gaussian KDE regressions, while the shaded areas represent the 1$\sigma$ confidence intervals of the regressions. The gray dashed line represents the solar value of [Ba/Eu].

# Chapter 5

# Conclusions

In order to understand the efficiency of the r-process in the LMC and compare it with that of the SMC, we re-measured the chemical composition of 113 stars located in the inner bar of the LMC. In particular, our analysis exploits the recent and precise photometry provided by the Data Release 3 of the Gaia Mission. Also, to remove any systematics that could arise from the main assumptions of the chemical analyses (computation of the stellar parameters, model atmospheres, atomic data, etc.) we adopted the same assumptions and procedures applied for the SMC in Anoardo et al. (2026).
Aside from Fe abundances, also Eu, Mg and Ba abundances were derived, in order to investigate and compare the efficiencies of the r-process, the $\alpha-$capture process, and the s-process respectively.
The main results are summarized as follows:

- The LMC stars exhibit enhanced [Eu/Fe] abundance ratios, with a clear decrease as the metallicity increases. These high [Eu/Fe] abundance ratios reflect the strong efficiency of the r-process in this galaxy. A comparison with the SMC and the Milky Way highlights that [Eu/Fe] values in the LMC are similar to those of the SMC, and slightly higher (by $\sim$ 0.1 dex) than those measured in the Milky Way stars of the same [Fe/H]. The decreasing trend from [Fe/H]$\gtrsim -1.5$ dex marks the onset of SNe Ia polluting the ISM with Fe but without producing Eu.

- The LMC shows a decline of [Mg/Fe] with [Fe/H], with enhanced values for the most metal-poor stars of the sample, and with solar-scaled values for most of the sample. This behaviour indicates that the stars were born in a gas already polluted by SNe Ia. The observed pattern is compatible with the theoretical models that predict a metal-poorer $\alpha-$knee for galaxies with a lower star formation efficiency than that of the Milky Way. With respect to the Milky Way, stars from the SMC and LMC appear to be depleted in [Mg/Fe], reflecting a lower contribution from massive stars to the enrichment of the ISM and a lower star formation efficiency in the Magellanic Clouds.

- The enhanced values of [Ba/Fe] in the LMC suggest that the s-process is also very efficient. Also, the increasing behaviour that is observed as a function of [Fe/H] is consistent with the onset of the s-process from AGB stars at delayed timescales. Comparing with the SMC, [Ba/Fe] is found to be similarly enhanced in the LMC and SMC, while Milky Way values are much lower, indicating a stronger contribution from AGB stars in the Magellanic Clouds.

- The LMC also exhibits high values for [Ba/Eu] abundances, demonstrating that the s-process is dominant with respect to the r-process.

- The LMC is characterized by enhanced [Eu/Mg] abundance ratios, similar to those measured in the SMC (Anoardo et al., 2026) and other dwarf spheroidal galaxies in the Local Group (see Reichert et al., 2020; Liberatori et al., 2025). On the other hand, results for [Eu/Mg] appear in stark contrast with respect to the Milky Way. The highest [Eu/Mg] that is observed in the LMC is the result of two combined effects: the [Eu/Fe] that is slightly enhanced with respect to the Milky Way, and the [Mg/Fe] that is significantly lower than that of Milky Way stars at the same [Fe/H]. This indicates that the r-process is more efficient than the $\alpha-$capture process in the LMC (and in other dwarf galaxies).

- To qualitatively interpret the Eu abundances in the LMC, we can use the same theoretical framework that was proposed for the SMC (Palla et al., 2026) and for other dwarf galaxies (Palla et al., 2025). In galaxies with a lower star formation efficiency, chemical evolution models predict significantly lower [Eu/Fe] and [Eu/Mg] abundance ratios with respect to the values that we observed. The only theoretical route proposed so far to reconcile models and observations, is to assume that these galaxies have had a higher frequency of NS mergers.

- Along with the SMC and other small galaxies of the Local group, the LMC shares the same tendency to have a more efficient r-process when compared to the $\alpha-$process. Consequently, the high [Eu/$\alpha$] seems to be a common characteristic of several galactic systems with low star formation efficiencies, likely similar to the former Milky Way satellites that were accreted and disrupted by the Galaxy. Therefore, this study confirms that [Eu/$\alpha$] is a valid tool for chemical tagging in the Milky Way, as stars that were accreted from dissolved systems (likely with chemical enrichment histories similar to those of the Magellanic Clouds and the dwarf spheroidal galaxies) are expected to exhibit enhanced [Eu/Mg] values.

As a result, the distinct trends of [Eu/Fe] and [Eu/Mg] observed in this work and displayed in other satellite galaxies of the Milky Way, support the idea to use these abundance ratios as tools to discriminate accreted stellar populations in the Galaxy. However, to fully exploit these results in the context of Galactic Archaeology, and in order to shed light into the assembly history of the Milky Way, further research to better understand neutron-capture processes in environments that exhibit different star formation efficiencies from the Galaxy is necessary. The next step in this research will be the calculation of tailored chemical enrichment models for the LMC in order to reproduce the observed chemical patterns.

# Bibliography


Abbott B. P., Abbott R., Abbott T. D., Acernese et al., 2017, *A gravitational-wave standard siren measurement of the Hubble constant*, Nature, 551, 85–88

Anoardo S., Mucciarelli A., Palla M., Santarelli L., Lardo C., Romano D., 2026, *The chemical DNA of the Magellanic Clouds: IV. Unveiling extreme element production: The Eu abundance in the Small Magellanic Cloud*, , 705, A31

Arcones A., Thielemann F.-K., 2023, *Origin of the elements*, , 31, 1

Arlandini C., Käppeler F., Wisshak K., Gallino R., Lugaro M., Busso M., Straniero O., 1999, *Neutron Capture in Low-Mass Asymptotic Giant Branch Stars: Cross Sections and Abundance Signatures*, The Astrophysical Journal, 525, 886

Burbidge E. M., Burbidge G. R., Fowler W. A., Hoyle F., 1957, *Synthesis of the Elements in Stars*, Rev. Mod. Phys., 29, 547

Busso M., Gallino R., Wasserburg G. J., 1999, *Nucleosynthesis in Asymptotic Giant Branch Stars: Relevance for Galactic Enrichment and Solar System Formation*, , 37, 239

Ceccarelli E., Mucciarelli A., Massari D., Bellazzini M., Matsuno T., 2024, *A comparative high-resolution spectroscopic analysis of in situ and accreted globular clusters*, , 691, A226

Cowan J. J., Sneden C., Lawler J. E., Aprahamian A., Wiescher M., Langanke K., Martínez-Pinedo G., Thielemann F.-K., 2021, *Origin of the heaviest elements: The rapid neutron-capture process*, Reviews of Modern Physics, 93, 015002

Cristallo S., Straniero O., Piersanti L., Gobrecht D., 2015, *Evolution, Nucleosynthesis, and Yields of AGB Stars at Different Metallicities. III. Intermediate-mass Models, Revised Low-mass Models, and the ph-FRUITY Interface*, , 219, 40

Erkal D., et al., 2019, *The total mass of the Large Magellanic Cloud from its perturbation on the Orphan stream*, , 487, 2685

Gaia Collaboration et al., 2021, *Gaia Early Data Release 3. Summary of the contents and survey properties*, , 649, A1

Gaia Collaboration Vallenari, A. Brown, A. G. A. Prusti, T. de Bruijne, J. H. J. Arenou, F. 2023, *Gaia Data Release 3 - Summary of the content and survey properties*, A&A, 674, A1

Gallino R., Arlandini C., Busso M., Lugaro M., Travaglio C., Straniero O., Chieffi A., Limongi M., 1998, *Evolution and Nucleosynthesis in Low-Mass Asymptotic Giant Branch Stars. II. Neutron Capture and the S-Process*, , 497, 388

Hasselquist S., et al., 2021, *APOGEE Chemical Abundance Patterns of the Massive Milky Way Satellites*, , 923, 172

Kobayashi C., Karakas A. I., Lugaro M., 2020, *The Origin of Elements from Carbon to Uranium*, , 900, 179

Kurucz R. L., 2005, *ATLAS12, SYNTHE, ATLAS9, WIDTH9, et cetera*, Memorie della Societa Astronomica Italiana Supplementi, 8, 14

Lattimer J. M., Schramm D. N., 1974, *Black-Hole-Neutron-Star Collisions*, , 192, L145

Liberatori A., Alvarez Garay D. A., Palla M., Mucciarelli A., Bellazzini M., Romano D., 2025, *A chemical close-up of the main body of the Sagittarius dwarf galaxy*, , 699, A356

Matteucci F., Greggio L., 1986, in Audouze J., Mathieu N., eds, NATO Advanced Study Institute (ASI) Series C Vol. 163, Nucleosynthesis and its Implications on Nuclear and Particle Physics. pp 315–323

Matteucci F., Romano D., Arcones A., Korobkin O., Rosswog S., 2014, *Europium production: neutron star mergers versus core-collapse supernovae*, , 438, 2177

Molero M., Magrini L., Matteucci F., Romano et al., 2023, *Origin of neutron-capture elements with the Gaia-ESO survey : the evolution of s- and r-process elements across the Milky Way*, MNRAS, 523

Monty S., et al., 2024, *The ratio of [Eu/α] differentiates accreted/in situ Milky Way stars across metallicities, as indicated by both field stars and globular clusters*, , 533, 2420

Mösta P., Roberts L. F., Halevi G., Ott C. D., Lippuner J., Haas R., Schnetter E., 2018, *r-process Nucleosynthesis from Three-dimensional Magnetorotational Core-collapse Supernovae*, , 864, 171

Mucciarelli A., 2011, *Microturbulent velocity from stellar spectra: a comparison between different approaches*, , 528, A44

Mucciarelli A., Bonifacio P., 2020, *Facing problems in the determination of stellar temperatures and gravities: Galactic globular clusters*, , 640, A87

Mucciarelli A., Bellazzini M., Massari D., 2021, *Exploiting the Gaia EDR3 photometry to derive stellar temperatures*, , 653, A90

Mucciarelli A., Minelli A., Bellazzini M., Lardo C., Romano D., Origlia L., Ferraro F. R., 2023, *The chemical DNA of the Magellanic Clouds. I. The chemical composition of 206 Small Magellanic Cloud red giant stars*, , 671, A124

Nidever D. L., et al., 2020, *The Lazy Giants: APOGEE Abundances Reveal Low Star Formation Efficiencies in the Magellanic Clouds*, , 895, 88

Oemler Jr. A., Tinsley B. M., 1979, *Type I supernovae come from short-lived stars.*, , 84, 985

Pagel B. E. J., Tautvaisiene G., 1998, *Chemical evolution of the Magellanic Clouds: analytical models*, , 299, 535

Palla M., Molero M., Romano D., Mucciarelli A., 2025, *Europium, we have a problem: Modelling r-process enrichment across Local Group galaxies*, , 699, A209

Palla M., Mucciarelli A., Romano D., Anoardo S., Matteucci F., 2026, *The chemical DNA of the Magellanic Clouds: VI. Origin and evolution of neutron-capture elements in the SMC*, , 710, A45

Pasquini L., et al., 2000, in Iye M., Moorwood A. F., eds, Society of Photo-Optical Instrumentation Engineers (SPIE) Conference Series Vol. 4008, Optical and IR Telescope Instrumentation and Detectors. pp 129–140, doi:10.1117/12.395491

Pian E., et al., 2017, *Spectroscopic identification of r-process nucleosynthesis in a double neutron-star merger*, , 551, 67

Pompéia L., et al., 2008, *Chemical abundances in LMC stellar populations. I. The inner disk sample*, , 480, 379

Reichert M., Hansen C. J., Hanke M., Skúladóttir Á., Arcones A., Grebel E. K., 2020, *Neutron-capture elements in dwarf galaxies. III. A homogenized analysis of 13 dwarf spheroidal and ultra-faint galaxies*, , 641, A127

Reichert M., Obergaulinger M., Eichler M., Aloy M. Á., Arcones A., 2021, *Nucleosynthesis in magneto-rotational supernovae*, , 501, 5733

Rubele S., et al., 2018, *The VMC survey - XXXI: The spatially resolved star formation history of the main body of the Small Magellanic Cloud*, , 478, 5017

Skrutskie M. F., et al., 2006, *The Two Micron All Sky Survey (2MASS)*, , 131, 1163

Soker N., 2026, *The early r-process nucleosynthesis scenarios*, arXiv e-prints, p. arXiv:2601.15187

Stanimirović S., Staveley-Smith L., Jones P. A., 2004, *A New Look at the Kinematics of Neutral Hydrogen in the Small Magellanic Cloud*, , 604, 176

Suda T., et al., 2008, *Stellar Abundances for the Galactic Archeology (SAGA) Database — Compilation of the Characteristics of Known Extremely Metal-Poor Stars*, , 60, 1159

Thielemann F.-K., Cowan J. J., 2026, *The r-process: history, required conditions, astrophysical sites, and observations*, European Physical Journal A, 62, 105

Van der Swaelmen M., Hill V., Primas F., Cole A. A., 2013, *Chemical abundances in LMC stellar populations. II. The bar sample*, , 560, A44

Watson D., et al., 2019, *Identification of strontium in the merger of two neutron stars*, , 574, 497

Woosley S. E., Heger A., 2006, in Holt S. S., Gehrels N., Nousek J. A., eds, American Institute of Physics Conference Series Vol. 836, Gamma-Ray Bursts in the Swift Era. AIP, pp 398–407 (arXiv:astro-ph/0604131), doi:10.1063/1.2207927

van der Marel R. P., Kallivayalil N., 2014, *Third-epoch Magellanic Cloud Proper Motions. II. The Large Magellanic Cloud Rotation Field in Three Dimensions*, , 781, 121